A COMPUTATIONAL FRAMEWORK FOR THE PREDICTION OF MULTISTAGE HEAT TREATMENTS IN AGE HARDENED ALLOYS

A Thesis

by

LUKE AARON JOHNSON

Submitted to the Office of Graduate and Professional Studies of
Texas A&M University
in partial fulfillment of the requirements for the degree of

MASTER OF SCIENCE

Chair of Committee,	Raymundo Arróyave
Committee Members,	Ibrahim Karaman
	Richard Malak
Head of Department,	Ibrahim Karaman

December 2015

Major Subject: Materials Science and Engineering

ABSTRACT

The computer-aided materials design process, otherwise known as Integrated Computational Materials Engineering (ICME), is highly iterative and as such requires flexible tools that have the ability to link processing, properties, and performance not only in the usual forward direction but also in the inverse direction more associated with a goal-oriented/design framework of ICME. While many techniques exist that relate properties to performance in both forward/inverse directions, tools that prescribe a process when given a desired microstructure have not been developed in detail. This research fills that gap by coupling physics-based precipitation models with "mesh adaptive direct search" optimization techniques. The tool is used to prescribe heat treatments in Ni-rich NiTi shape memory alloys that will result in a desired size distribution of Ni_4Ti_3 precipitates. This predictive technique provides a rigorous strategy for the identification of materials processing schedules—provided the forward models connecting processing and microstructure are available—that can significantly reduce the experimental search space that needs to be explored, accelerating the materials development process.

DEDICATION

For my family and friends. Thank you for the unforgettable memories and amazing opportunities that have shaped me into the person I am today.

ACKNOWLEDGEMENTS

I would like to thank all of my co-workers and collaborators who helped throughout the course of this research. The individual contributions from each person are too numerous to list here, so all I will simply say that everyone I have had the pleasure of meeting during my time here has become both a friend and a mentor in some way or another, whether they realize it or not. This research wouldn't have been possible without the support of each and every one of them.

NOMENCLATURE

MGI	Materials Genome Initiative
NOMAD	Nonlinear Optimization with Mesh Adaptive Direct Search
PSD	Precipitate Size Distribution
KS	Kolmogorov-Smirnov
CS	Chi-Squared
SMA	Shape Memory Alloy
SME	Shape Memory Effect
SE	Super Elastic
Ni	Nickel
Ti	Titianium
B2	Ordered BCC Crystal Structure
Ni_4Ti_3	Metastable Precipitate (Intermetallic)
$B19'$	Monoclinic Martensite
$R-Phase$	Intermediate $P\bar{3}$ Trigonal Phase in Martensitic Transformation
DSC	Differential Scanning Calorimetry
Ni_3Ti_2	Metastable Precipitate (Intermetallic)
TTP	Time-Temperature-Precipitation Diagram
MatCalc	Precipitation Simulation Software
NKW	Numerical Kampmann Wagner Growth Model
CNT	Classical Nucleation Theory
J	Nucleation Rate
N	Number of Nucleation Sites
β^*	Attachment Rate Term

τ	time lag (incubation constant)
T	temperature
k_B	Boltzmann's Constant
G^*	Critical Gibbs Energy for Nucleation
v	Interface Velocity
J_X^{ij}	Flux of Component X from Phase i to Phase j
C_X^{ij}	Composition of component X on i Side of ij Interface
SFFK	Precipitate Growth Model (multicomponent, multiphase)
TEP	Thermodynamic Extremum Principle
L	Mechanical Analog to Gibbs Energy (G) (Driving Force)
F	Mechanical Dissipation
G	Gibbs Free Energy
$Q_{1,2,3}$	Thermodynamic Dissipative Forces
q_i	Precipitate Variable (typically radius)
$\dot{q}_i$	Precipitate Rate variable (typically radial growth rate)
N_{0i}	Number of i Atoms in Matrix
$\mu_{0i,ki}$	Chemical Potential of Component i in Matrix or Precipitate k
n	Number of Components
λ_k	linear misfit term
δ_k	Interfacial Energy of Precipitate k
$\dot{C}_{0i,ki}$	Rate of Change of Component i in Matrix or Precipitate k
R	Ideal Gas Constant
λ	Lagrange Multiplier
ρ_k	Radius of Precipitate
$C_{0i,ki}$	Composition of Component i in Matrix or Precipitate k

$D_{0i,ki}$	Diffusion Coefficient of Component i in Matrix or Precipitate k
δ_{ij}	Kronecker Delta
M_{IF}	Interface Mobility
a_{kij}	Constraint Coefficients Between Component i and j in Precipitate k
LS	Langer-Schwartz Precipitate Growth Model
CDF	Cumulative Size Distribution
$F_i(r)$	Continuous Cumulative Distribution Function for Distribution i
$\bar{F}_i(r)$	Step Cumulative Distribution Function for Distribution i
$\tilde{F}_i(r)$	Trapezoidal Cumulative Distribution Function for Distribution i
$f_i(r)$	Continuous Precipitate Size Distribution for Distribution i
$\bar{f}_i(r)$	Step Precipitate Size Distribution for Distribution i
$\tilde{f}_i(r)$	Trapezoidal Precipitate Size Distribution for Distribution i
D_{CS}	Chi-Squared Fitness Value
D_{KS}	Kolmogorov-Smirnov Fitness Value
$\Delta f_i(r)$	Difference between CDFs at Radius r
T_1	Temperature of First Stage of Heat Treatment
t_1	Time of First Stage of Heat Treatment
T_2	Temperature of Second Stage of Heat Treatment
t_2	Temperature of Second Stage of Heat Treatment
MADS	Mesh Adaptive Direct Search
GPS	Generalized Pattern Search
VNS	Variable Neighborhood Search
LH	Latin Hypercube Search Method

TABLE OF CONTENTS

Page

LIST OF FIGURES

FIGURE Page

FIGURE Page

LIST OF TABLES

TABLE Page

1. INTRODUCTION: MATERIALS DESIGN

1.1 Current State of the Art

The Materials Genome Initiative (MGI) [11] has informed and guided research in Materials Science since its release. One emphasis of the MGI is that it is imperative to decrease deployment time of new materials by including materials design in the overall design process of consumer products. The key to successful materials design integration is the development of a top-down design approach in the context of the process-properties-performance hierarchy (PPP) shown in Fig. 1.1. The bottom-up forward materials science research direction subjects raw materials to predefined processes that results in a microstructure which possesses properties that are analyzed to predict performance metrics. In contrast, the top-down design direction uses performance criteria to determine the necessary properties and therefore microstructure of a material, which is subsequently used to discover the necessary processing steps.

The first link (between performance and properties) has been well characterized over the years through both experimental and computational approaches, but models which predict processing based on a desired microstructure are often missing from the top-down design framework. While this final link between raw materials and microstructure could be determined through iterative experimental work, a computational approach makes much more sense in the context of accelerated materials design.

1.2 This Work's Contribution

Solving the (inverse) connection between (micro)structure and chemistry + processing is still quite challenging in the general sense, and the problem can only be addressed in some very specific circumstances. As a contribution to this problem,

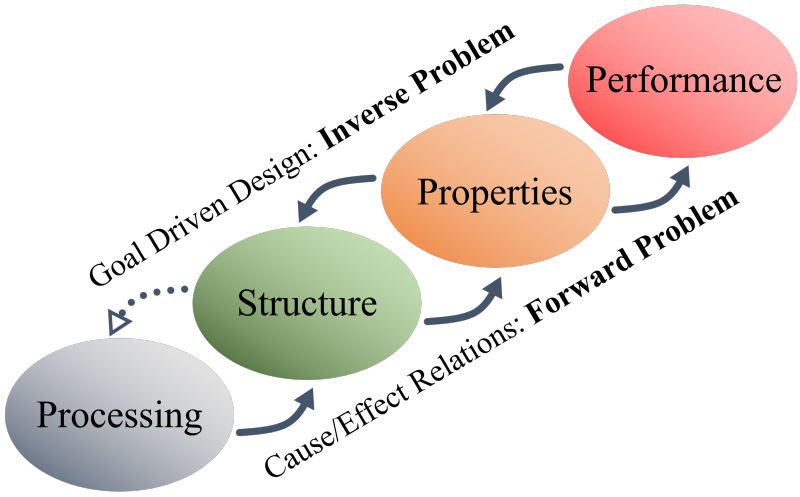

Figure 1.1: The forward and inverse problems in materials science development [40]. The dashed arrow shows the gap in goal driven material design that this research fills, particularly in the context of precipitation aged systems.

this paper details a computational materials science framework which can provide that last link (as seen in Figure 1.1) for top-down material design by predicting the processing steps required to achieve application-specific microstructures, assuming that such microstructures have already been determined through experimental or computational means.

In brief, the proposed framework uses advanced, thermodynamics and kinetics-based multi-component, multi-phase precipitation modeling [66], in conjunction with mesh adaptive direct search techniques (NOMAD [40]) to prescribe multi-stage heat treatments that result in a desired precipitate size distribution (PSD). The framework borrows some ideas and concepts from genetic programming whereby instead of optimizing a function, what is optimized is a specific sequence of steps encoded in terms of a multi-dimensional parameter space. Fitness of a candidate heat treatment is assessed by comparing its resulting PSD to a target PSD using elements from different

statistical techniques such as the Kolmogorov-Smirnov (KS) [43] and/or Chi-Squared tests.

Quite possibly the most important point of this work is that although this framework was developed in the context of heat treatment prediction in Nickel-Titanium alloys, there is no reason it cannot be applied to any material that has properties best described by distributions, as long as an appropriately calibrated material model is used and a target distribution is available for the relevant property. Approaches such as materials optimization via Microstructure Sensitive Design [16] address the connectivity between properties/performance and microstructure.

1.3 Motivation for Material Selection

Shape Memory Alloys (SMAs) exhibit the so-called shape memory effect (SME) and superelasticity (SE) as a result of reversible thermoelastic martensitic transformations. NiTi-based systems are among the most promising SMAs for engineering and biomedical applications thanks to their one-way effect and pseudoelasticity [42]. The martensitic transformation temperatures in SMAs should fall close to the operating temperatures of the part and in the case of NiTi SMAs they are highly dependent on the process (heat treatment) history of the material due to strong sensitivity to composition [15]. This sensitivity makes NiTi SMAs incredibly tailorable to many useful engineering applications.

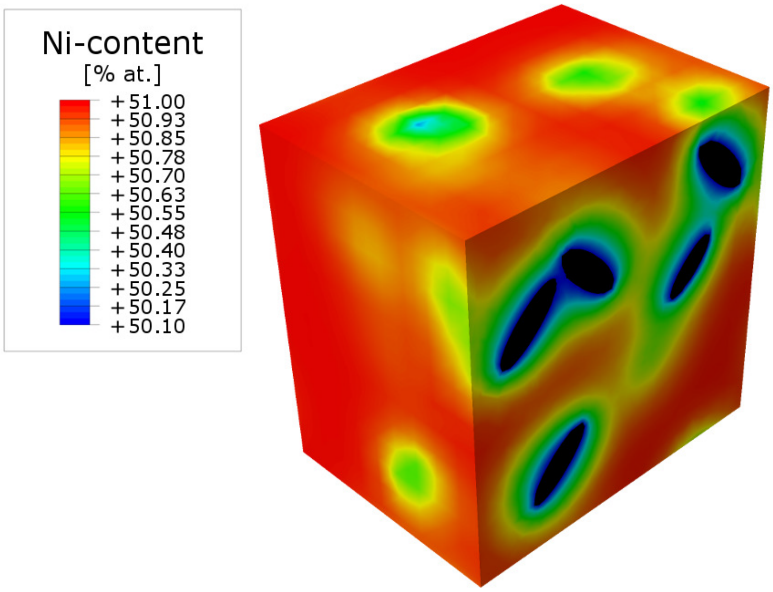

Figure 1.2: Phase field model showing regions of Ni depletion in the matrix surrounding Ni-rich precipitates [9].

In addition to altering the composition of the surrounding matrix (seen in Figure 1.2) [68, 9], the presence of precipitates in the system adds an entirely new set of influences on the transformation characteristics of the bulk material. One of the most notable influences of precipitation on martensitic transformations in NiTi SMAs is the appearance of intermediate phase(s) between the B2 austenite phase and the B19' martensite phase after aging. Evidence of the transformations between these intermediate phase(s) can be seen as additional peaks in the Differential Scanning Calorimetry (DSC) curves of aged materials. DSC is an experimental technique that compares the heat transfer rate of an aged NiTi sample to some reference material over a range of temperatures. There are many examples of DSC curves in the literature which show transformations of NiTi alloys at varying stages of aging. Some of DSC curves of aged NiTi alloys show three peaks which would typically indicate the

appearance of another matrix phase but it has been shown, through DSC curve comparisons between aged single crystals and polycrystals, that the extra peak is due to the heterogeneity of the crystal structure brought about by preferential precipitation along grain boundaries [24, 3, 13]. This result essentially means that transformation temperature(s) vary spatially in the grain.

Another study compared precipitation of single and polycrystals, with and without the influence of 50 MPa compressive external stresses to confirm this preferential grain boundary precipitation, as well as elucidate the driving force behind it (relaxation of internal stresses localized near grain boundaries) [35]. Homogeneous nucleation was obtained in single crystals at all external stress levels and exhibited preferential nucleation of a single variant perpendicular to the applied stress, further emphasizing the effect of stresses on precipitation [35]. Polycrystalline NiTi samples have also been shown to exhibit homogeneous nucleation at a threshold external stress of as little as 2 MPa, but often show three peaks on their DSC curves, most likely due to the presence of multiple orientational variants of Ni_4Ti_3 in each grain [23, 35].

So far, the mere presence of the particles has been discussed as the influencing factor in NiTi SMA transformation pathways, but their size is also a major factor in the behavior of the system. This is due to the direct effect of a reduction of excess Ni in the matrix as the precipitates grow and nucleate. The precipitates can also limit the development of plastic accumulation by inhibiting dislocation motion if they are smaller than 15 [nm] with appropriate inter-particle spacing [25].

1.3.1 Motivation Summary

The wide range of case-dependent influences linked to the various phase characteristics above shows that precipitation alone can drastically influence the entire

transformation response of a NiTi SMA. Unfortunately, the cost associated with the identification of the relationships between heat treatment parameters and microstructure are so high that the usual approach to the deployment of NiTi SMAs in application is limited to the design of the actuation mechanism around off-the-shelf alloys, with predetermined transformation behavior. This approach reduces the flexibility necessary for the rapid adoption of active materials in wider range of technologies. Taking all of these factors into consideration shows that this system a perfect candidate for the process prediction framework detailed over the course of this thesis.

2. MATERIALS MODELING

This section focuses on the Ti - 52at%Ni system analyzed in this research as well as the thermodynamic and kinetic theories that make up the model used to characterize the evolution of the system. The section is comprised of five sections, the first of which briefly describes the Ni_4Ti_3 precipitate in the context of NiTi SMAs. The next three sections describe the nucleation, growth and coarsening strategies underlying the precipitation model, followed by a section which talks about the numerical implementation of those theories. The modeling section is wrapped up with the calibration of the model to an experimental heat treatment that results in a bi-modal distribution which is subsequently used as the prediction framework's target distribution.

2.1 Precipitation System Discussion

As touched upon in the introduction, NiTi shape memory alloys are useful in a number of applications because of the tailorability of their temperature induced reversible martensitic phase transformations through the nucleation and growth of precipitates. Formation and growth of Ni-rich precipitates such as Ni_4Ti_3 reduces the nominal Ni content of the matrix which drastically affects the system's M_s temperature [39, 42, 48, 56, 47]. It has also been shown that coherent Ni_4Ti_3 precipitates influence the transformation paths of the matrix through precipitate-lattice mismatch induced strain energy [39, 8, 67, 58, 57, 68]. This lattice mismatch surrounding Ni_4Ti_3 precipitates alters the free energy of the surrounding matrix through elastic strain contributions and local variations in Ni concentration.

One view states that the coherent strain energy affects phases with large lattice transformations (B19') more than phases with small lattice transformations (R-

phase). This differential decrease in stability between B19' and R-phase in response to the local strain energy surrounding Ni_4Ti_3 precipitates leads to the intermediate stability of R-phase and its subsequent appearance in the middle of the B2-B19' transformation path (B2-R-B19') [47]. A similar but alternate viewpoint suggests that the differential effect of Ni_4Ti_3 precipitates on the stability of the two phases is due local regions of thermodynamically preferential Ni content and lattice strain surrounding the precipitate, which are spatially coincident for the R-phase but not the B19' phase [68].

In any case, the Ni_4Ti_3 induced R-phase is desirable for its small thermal hysteresis and resistance to cyclic fatigue, which make it an excellent candidate for use in actuation applications [36, 18, 51, 26]. Although the Ni_3Ti_2 and Ni_3Ti_1 precipitates are more stable, they are often considered detrimental and are therefore eliminated/ignored during the kinetic simulations of this research by limiting the search space to times and temperatures indicated by the shaded region in Figure 2.1 [38].

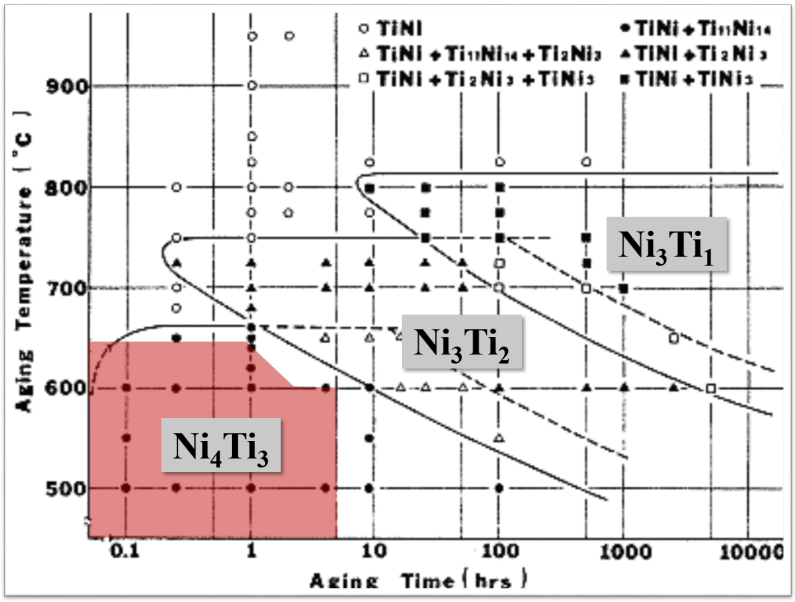

Figure 2.1: TTP diagram for the binary NiTi system. The shaded area shows the approximate region of times and temperatures this research will be analyzing [38].

All precipitation simulations in this research are performed with the kinetic simulation software MatCalc [27]. The kinetic evolution of precipitation reactions can be broken into three distinct stages: nucleation, growth, and coarsening. Many models have been developed for each of these stages to more accurately capture some of the various types of precipitate evolution. The next three sections (2.2 - 2.4) will be devoted to detailing the thermodynamic and kinetic theories behind MatCalc's modeling approach in each of those stages. It is important to remember that even though these stages are traditionally thought of as being completely sequential, they often occur simultaneously.

2.2 Nucleation

2.2.1 Origins of Nucleation Theory

The original solid-state nucleation models in materials science were inspired by the Classical Nucleation Theory (CNT) used to describe the nucleation behavior of liquid droplets from supersaturated vapor systems that are cooled to a temperature below their solvus /cite. With CNT, a system is characterized by its nucleation barrier which is the result of size-dependent contributions to the free energy of a droplet, based on its volume and surface area. The probability of overcoming that barrier and having a nucleation event (i.e. nucleation rate J) can be seen in (Equation 2.1).

$$J = NZ\beta^* e^{\frac{-G^*}{k_B T}} e^{\frac{-\tau}{T}} \tag{2.1}$$

Where the Z term is the Zeldovich factor that uses information about the curvature (2^{nd} derivative) of the free energy to characterize the possibility of random walk nucleation through fluctuations in the system, (β^*) is the attachment rate term that accounts for kinetic influences such as diffusivity in the matrix and the interface, and the exponential term encapsulates the direct contributions from the temperature-dependent free energy of the droplet. N is simply the number of possible nucleation sites, and the time dependent exponential term (τ) is sometimes added to account for the time lag associated with the non steady-state condition of cooling from an overheated initial state to some temperature below the solvus line [63, 14].

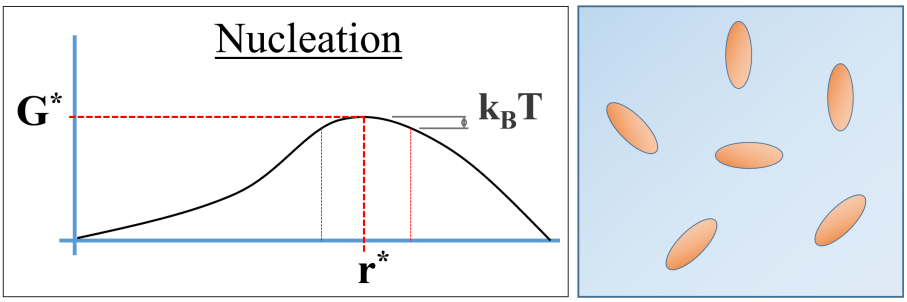

Figure 2.2: Schematic of solid state nucleation and plot of energy as a function of precipitate radius showing critical barrier for nucleation.

2.2.2 Solid State Nucleation Theory

The addition of more terms to the exponential free energy term is really what differentiates vapor-liquid and solid-solid CNT. These terms can account for anything that changes the free energy of the system such as the matrix-precipitate volumetric misfit or thermodynamic contributions from excess vacancies, neither of which exist in isobaric liquid-vapor transformations. Volumetric misfit contributions to the free energy are determined through Eshelby's model for elastic stress fields around an inclusion [12].

Heterogeneous nucleation affects the number of nucleation sites N and also modifies the free energy nucleation barrier either positively or negatively depending on the volumetric misfit and/or interfacial energy of the precipitating phase. To estimate the number of heterogeneous nucleation sites in a system, MatCalc uses various analytical techniques such as dislocation density and/or geometric objects called Kelvin cells to approximate the number of nucleation sites on grain boundary edges, faces, and corners [27].

2.3 Growth

The modeling of precipitate growth in solid state phase transformations can be classified into two main approaches. A brief review of the standard diffusion controlled approach will be given, followed by a more in-depth discussion of the mean field approach utilized in the MatCalc simulations for this research.

2.3.1 Diffusional Approach

The simplest approach to modeling precipitate evolution is to frame the growth of a precipitate as a moving boundary problem that ultimately seeks to determine the interface position and velocity v (i.e. evolution of precipitate radii). It does this through the application of mass balance equations that include terms to describe the fluxes in each phase as well as elemental concentrations on either side of the precipitate-matrix interface. (Equation 2.2) shows an example of a general velocity equation for a binary system in which the growth of β phase precipitates in an α matrix are governed by the diffusion of element B.

$$v = \frac{J_B^{\alpha\beta} + J_B^{\beta\alpha}}{[c_B^{\beta\alpha} + c_B^{\alpha\beta}]} \tag{2.2}$$

In addition to the mass balance equations, many models make the assumption that diffusion across the interface is rapid enough to consider that region of the system to be in local equilibrium, implying that the flux of components across the interface and the movement of the interface itself possess no dissipative properties. Accurately modeling precipitate growth with this technique is difficult because the main assumptions used to determine the flux terms on either side of the interface are based on the difference in precipitate-matrix interface concentrations. Since this concentration difference changes in time as well, the system may evolve into a state

in which the governing equations, based on the initial concentration difference, are no longer valid.

More thorough approaches consider dissipative effects of the interface in conjunction with long range diffusion in the precipitate and matrix [50]. While these models are more precise than the simple local equilibrium approach above, they are often tailored to relatively narrow ranges of system parameters which inevitably evolve over the course of the phase transformation, necessitating the evolution or switching of models dynamically during the simulation, further increasing their complexity.

2.3.2 Mean Field Approach

An alternative approach to these two diffusion-controlled growth models is called the SFFK model [53] which is a mean-field approach based on the Thermodynamic Extremal Principle (TEP). For a more comprehensive derivation of TEP and the SFFK model, the reader is referred to Kozeschnik's book Modeling Solid-State Precipitation [28]. The TEP essentially states that a system out of equilibrium at constant temperature and pressure will evolve along the path of maximum Gibbs energy dissipation rate (maximum entropy production) subject to the governing equation (Equation 2.4) [41]. The TEP equation has been derived in a couple ways, the most elegant approach uses the analogous Lagrange equation(s) from classical mechanics (Equation 2.3).

$$\frac{\partial L}{\partial q_i} - \frac{d}{dt}\left(\frac{\partial L}{\partial \dot{q}_i}\right) = \frac{\partial F}{\partial \dot{q}_i} \tag{2.3}$$

$$\frac{\partial G}{\partial q_i} = \frac{-\partial Q}{2\partial \dot{q}_i} \tag{2.4}$$

To transform from the mechanical equation (2.3) to the chemical equation (2.4) above, a few analogies between the systems must be made [54]. The mechanical term L representing the kinetic/potential energy difference of the mechanical system

is analogous to the thermodynamic term G which represents the Gibbs free energy of the system. The mechanical dissipative force F is analogous to Q, the total energy dissipation rate of the chemical system. The variables q_i and $\dot{q}_i$ in the mechanical equation (2.3) represent position and velocity of the i^{th} degree of freedom. Similarly, q_i in the chemical equation (2.4) represents variables such as composition and/or precipitate radius while $\dot{q}_i$ represents diffusional flux and/or radius growth rate terms.

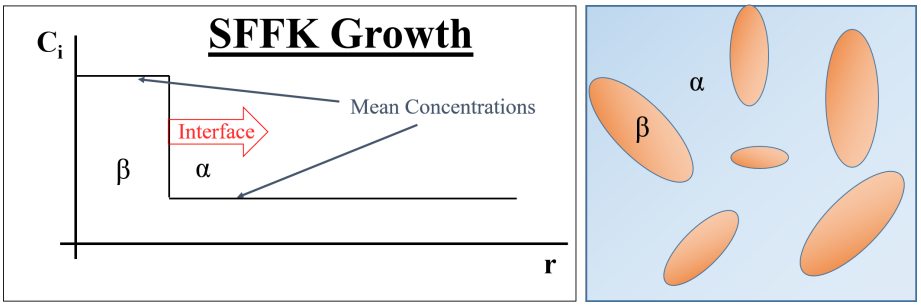

Figure 2.3: Mean Field concentration profile for growth of precipitates in a solid state material.

2.3.2.1 Energetic Contributions: Thermodynamics

The Gibbs energy equation (2.5) is constructed through a linear superposition of three terms that account for i) energy contributions of the matrix ii) energy contributions from the precipitate inside the matrix, and energy contributions associated with the precipitate-matrix interface [29]. The matrix contributes energy in the form of chemical potential; the precipitate also contributes energy through chemical potential, but adds an additional accounting for the volumetric misfit of the precipitate inside the matrix; the interfacial energy term is just the interfacial energy of the precipitate-matrix interface multiplied by the total surface area between all

precipitates and the surrounding matrix [1].

$$G = \sum_{i=1}^{n} N_{0i}\mu_{0i} + \sum_{k=1}^{m} \frac{4\pi\rho_k^3}{3}\left(\lambda_k + \sum_{i=1}^{n} c_{ki}\mu_{ki}\right) + \sum_{k=1}^{m} 4\pi\rho_k^2\gamma_k \tag{2.5}$$

2.3.2.2 Dissipative Contributions: Kinetics

The overall dissipative equation is a linear superposition of three terms which account for the friction of interfacial movement, diffusion of elements in the precipitate, and diffusion of elements in the matrix. It's worth noting that the mean-field basis of this approach (Figure 2.3) is based on the assumption that concentration profiles are constant in both the precipitate and matrix phases which simplifies the derivation and following equations by eliminating integrations with respect to the radius of each particle.

$$Q_1 = \sum_{k=1}^{m} \frac{4\pi\rho_k^2}{M_k^{IF}}\dot{\rho}_k^2 \tag{2.6}$$

$$Q_2 = \sum_{k=1}^{m}\sum_{i=1}^{n} \frac{4\pi RT\rho_k^5\dot{c}_{ki}^2}{45c_{ki}D_{ki}} \tag{2.7}$$

$$Q_3 = \sum_{k=1}^{m}\sum_{i=1}^{n} \frac{4\pi RT\rho_k^3(\dot{\rho}_k(c_{ki} - c_{0i}) + \frac{\rho_k\dot{c}_{ki}}{3})^2}{c_{0i}D_{0i}} \tag{2.8}$$

2.3.2.3 Combined Equations and Constraints

The final evolution equations are specified by differentiating the Gibbs energy equation (2.5) with respect to composition and precipitate radius; the overall dissipation equation $Q = Q_1 + Q_2 + Q_3$ is differentiated as well, but with respect to the

[1] All of these equations are derived assuming spherical precipitates, but MatCalc has implemented a shape factor feature, which alters the equations to reflect different volume and surface area coefficients based on aspect ratio.

rate of change of composition and precipitate radius. Additional constraints such as precipitate stoichiometry are then added to the set of equations in the form of Lagrange multipliers. Finally, the set of equations for each precipitate may be separated, linearized and represented by two instances of the following equation (2.9) where q_i represents concentration in one equation and precipitate radius in the other.

$$\frac{\partial}{\partial \dot{q}_i}\left[Q = \lambda(\dot{G} + Q) + \sum_{k=1}^{m}\sum_{j=1}^{p_k} v_{kj} \sum a_{kij}\dot{c}_{ki}\right] = 0, k = 1, ..., m \tag{2.9}$$

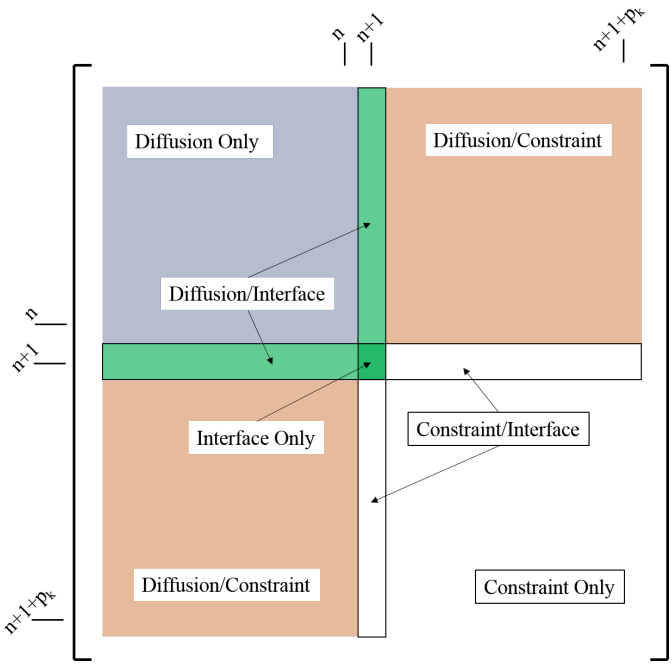

Figure 2.4: Matrix of coefficients for the linear system of growth equations. The different shaded areas show the significance of any coefficients located in those areas.

Table 2.1: Coefficient equations corresponding to the various regions of the Matrix seen in Figure 2.4.

Fill	Type	Equation	Eq. Num
	diff	$\frac{RT\rho_k^3}{45}\left(\frac{1}{c_{ki}D_{ki}}+\frac{5}{c_{0i}D_{0i}}\right)\delta_{ij}$	1
	const	$\frac{RT\rho_k^2}{3}\frac{c_{ki}c_{0i}}{c_{0i}D_{0i}}$	2
	int	$\frac{1}{M^{IF}}+RT\rho_k\sum_{i=1}^{n}\frac{(c_{ki}-c_{0i})^2}{c_{0i}D_{0i}}$	3
	diff/const	a_{kij}	4

That set of equations seems complicated, but if the matrix of coefficients visualized in terms of overlapping regions as shown in Figure 2.4 it becomes clear why the coefficients are populated in that particular manner. The blue and red regions represent the possible areas of the matrix where diffusional and constraint coefficients could be placed, respectively; the hashed region shows where the interfacial energy terms can be placed. The matrix has four distinct combinations of overlapping patterns and (Table 2.1) shows those combinations along with their meanings:

The purely hashed and red/hashed regions have no meaning in the context of this research for these reasons, respectively: i) constraint coefficients by themselves are meaningless and ii) stoichiometry constraints for an essentially amorphous interfacial region do not make sense. This leads to the conclusion that these two regions of the matrix need to be populated with zeros. Other regions will indeed include the coefficients specified in (Equations whole bunch) above. It is also interesting to note that the elimination of the Kronecker delta (δ) in (Equation 1 in Table 2.1) opens the possibility of off diagonal terms in the blue "diffusion only" zone, but cross diffusive

terms are not considered in this implementation.

2.4 Coarsening

Over the course of a precipitate phase transformation the average elemental content of the matrix changes due to mass conservation, reducing the driving forces for nucleation and growth. Although matrix compositions are typically reported as a single value average across the matrix, the Gibbs-Thompson equation [44] implies that there will be precipitate-size-dependent local inhomogeneities in the matrix composition surrounding each precipitate. Differences in the magnitudes of those inhomogeneities can lead to concentration gradients in the matrix as long as the precipitates are in close enough proximity. These concentration gradients cause atoms from smaller precipitates to diffuse toward larger ones (Figure 2.5) in a phenomenon often specifically referred to as Ostwald ripening [61] and more generally referred to as precipitate coarsening.

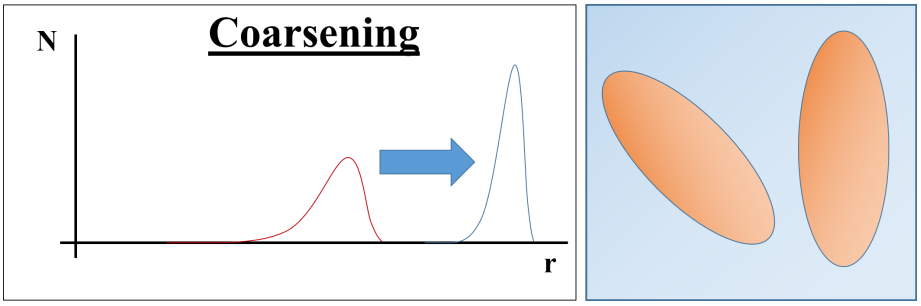

Figure 2.5: Schematic of coarsening behavior in a precipitate size distribution.

There are trade-offs to be considered when deciding which version of the Gibbs-Thompson equation to use in a precipitation model. As an example, one of the most common approximations eliminates quite a few terms in the general form by assuming

that the precipitate is entirely composed of the diffusing species B. This assumption is fine for compositionally distinct precipitates, but leads to large deviations, even if the composition of the precipitate drops to just 80 at% B [44].

The three sections of precipitate evolution discussed always start in the same sequence from nucleation to growth to coarsening, but there is no restriction saying that one stage has to stop before the other starts. In fact, they often overlap which can drastically affect the evolution of a system's precipitate size distribution. The two system parameters that determine whether these regions overlap are interfacial energy and supersaturation [49], which are any system's key kinetic and thermodynamic parameters, respectively. The extreme cases of overlapping nucleation, growth, and coarsening regimes are solely limited by either thermodynamics or kinetics.

2.5 Numerical Implementation: The NKW Method

As stated in the introduction to this section, MatCalc uses the NKW method to evolve the precipitation system in time [62]. This method extends the functionality of the previously developed Langer-Schwartz model [31] by representing the distribution as a set of discrete size classes instead of a continuous function. The NKW model also differs from the LS model in that the initial distribution of size classes is governed by the transient nucleation rate J of classical nucleation theory which is shown in (Equation 2.1). The use of an existing nucleation theory rather than the arbitrary distribution of the LS model allows for the effective modeling of all three major stages of precipitate evolution.

Once nucleated, the thermodynamic extremal principle (Section 2.3.2), subsequent SFFK governing equations (Section 2.3) and coefficients (Equation 2.9/Table 2.1) are used to determine the size evolution of each individual class at every time step. At the end of every time step the bin values of the size classes are re-evaluated

and the distribution is adjusted accordingly. The coarsening stage of particle evolution is introduced to the system through the NKW model's ability to redistribute and/or remove size classes that shrink below the critical radius of the system [28].

2.6 Model Calibration and Target Heat Treatment Development

Now that the theory behind the precipitation model has been established, the parameters of that model need to be calibrated by comparing its output with that of experiments. The distribution resulting from that calibration heat treatment is then decoupled from all of its processing information (times and temperatures) and serves as the target distribution of the prediction framework. This was necessary because no experimentally determined size distributions of Ni_4Ti_3 precipitates could be found in the literature. While using the calibration treatment as a target for prediction may slightly diminish the impact of the modeling portion of the prediction framework, it has no effect on the validity of the framework as a whole because it is the same as assuming perfect model calibration.

2.6.1 Experimental Heat Treatment

The selection of an experimental heat treatment with a bimodal distribution was deliberately chosen to showcase the advantages of using a size distribution metric over single value metrics for the comparison of precipitation aged microstructures, which will be discussed more in Section 3. The selected treatment consists of an initial high temperature stage at 550 [^{o}C] for 2 hours followed by a low temperature stage at 250 [^{o}C] for 5 hours [66]. This treatment resulted in larger Widmanstatten particles with sizes ranging from 0.2 - 0.8 [μm] and finely dispersed precipitates "two orders of magnitude smaller" as seen in Figure 2.6(a).

The calibration of this model consisted of altering key values in the governing equations shown above. As would be expected, the model is the most sensitive to

changes in interfacial energy γ, followed closely by changes to number of nucleation sites N. Calibrated values for these two parameters are 0.0505 [J/m^2] and 3 x 10^{29}, respectively. For a full list of parameters used in the calibration of this model, the reader is directed to the example script in Appendix A. The values seen in that script were determined by encoding the experimental heat treatment, then iteratively running the simulation while comparing the precipitate size distribution to the radii range from that heat treatment. These iterative calibration calculations consisted of systematic sweeps of each individual parameter (holding the other system parameters constant). This approach shed light on the isolated effect of each parameter, allowing for their feasible ranges to be narrowed down to the specific calibrated values seen in the appended script. The resulting distribution of this calibrated script can be seen in Figure 2.6.

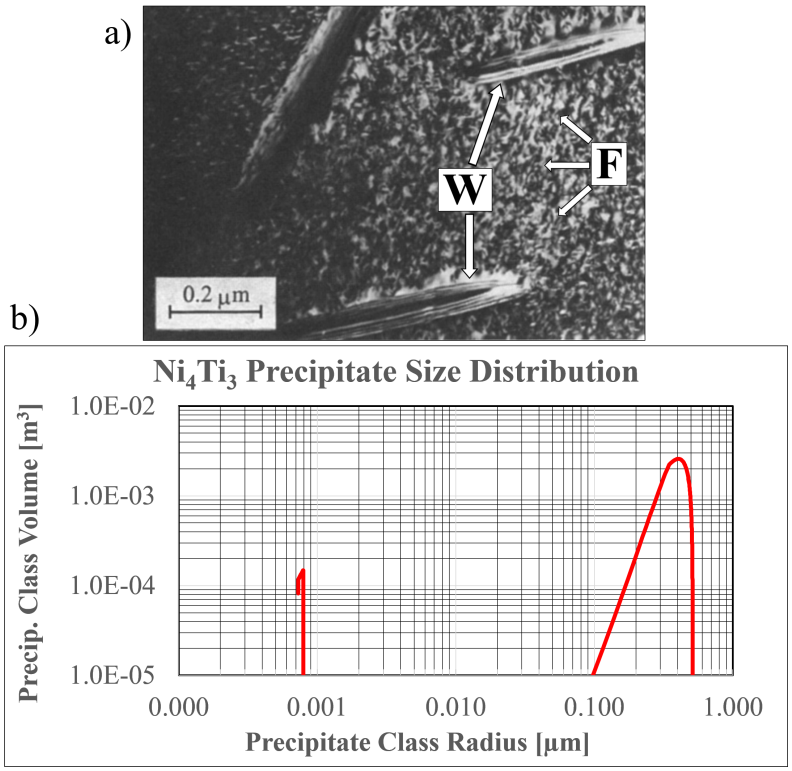

Figure 2.6: (a) Micrograph of a Ti - 52at%Ni system that has undergone a two stage heat treatment and (b) a size distribution calculated by the calibrated model. The treatment started at 550 [^{o}C] for 2 hours followed by 250 [^{o}C] for 5 hours, resulting in larger particles ranging from 0.2 - 0.8 [μm] and fine particles that are two orders of magnitude smaller [66].

2.6.2 Modeling Summary

In this section, details of the binary NiTi shape memory alloy system were given and the theories behind the governing equations of a few different nucleation, growth, and coarsening models were discussed, including the numerical implementation of those models. After the governing equations were established the calibration of those equations was undertaken by comparing their results to an experimentally created bimodal system of Ni_4Ti_3 precipitates. All processing information about

that calculated bimodal distribution will be discarded, leaving only the distribution which will now be considered as the target distribution of the predictive framework. Now that we have this target distribution, the next section (Section 3), will focus on developing a technique which can compare it to distributions from other heat treatments.

3. FITNESS EVALUATION TECHNIQUE

Now that a target distribution has been established, the task of rediscovering the heat treatment that produced that distribution can begin. This simulates an SMA design scenario that closely follows the goal-driven design path, seen in Figure 1.1, where the performance requirements of an alloy have already prescribed the required properties, which subsequently established a desired precipitate size distribution of Ni_4Ti_3 particles. At this structure checkpoint in the design process, the most common approach is to start conducting iterative experimental heat treatments on sample material, linking processing to structure from the bottom up which costs time and money. The top-down link from structure to processing can actually be established with computational techniques with an appropriate fitness metric that compares candidate heat treatment microstructures to those of the unknown target heat treatment.

This section explores the advantages of using the entire (predicted) precipitate size distribution as a metric used to gauge the fitness of a given thermal processing schedule, as opposed to traditional single-value properties. We show how the PSD can be transformed into the cumulative distribution function (CDF), which provides an even more efficient and robust statistical measure that can serve as a point of comparison between two distinct precipitate populations. A selection of relevant statistical comparison techniques, and their implementation in analogous size distribution applications, are described to inform the decisions which lead to the unique comparison technique used in the final optimization scheme of this research.

3.1 Justification for a Distribution Based Fitness Metric

As mentioned in the introduction of this section, the most important issue when trying to link structure to processing is the development of the criteria used to evaluate the fitness of the candidate solutions. When considering materials with precipitation-dependent properties, typical system descriptions and therefore fitness criteria are based on single-value material properties such as average radius and/or total number of precipitates [20, 46]. Using these properties as fitness criteria limits the effectiveness of the solution because many of these values possess degenerate solution spaces with multiple equally correct process pathways [16]. In addition to degeneracy, the single-value fitness evaluations are limited to unimodal systems since some properties such as mean radius lose physical meaning when the underlying microstructure possesses multimodal qualities. PSDs offer a solution to both of these problems because they i) encompass many more single-value properties than the ones listed above and ii) can be applied to systems with multimodal distributions [64].

As described in the Material Modeling section, MatCalc can output a PSD which reports the radius and number of precipitates for each size class. These two values are used to convert the PSD from number-based to volume-based bins, reducing the maximum difference in bin size from 10 to 3. From this volumetric reference frame it is fairly simple to see that the PSD does indeed include information about single-value properties. Adding all of the bin volumes from a system's PSD together results in the total volume fraction transformed as long as they are not normalized, which is required to maintain the physical relevance during the comparison. For example, two systems can have exactly the same normalized PSD, but completely different overall transformed volumes.

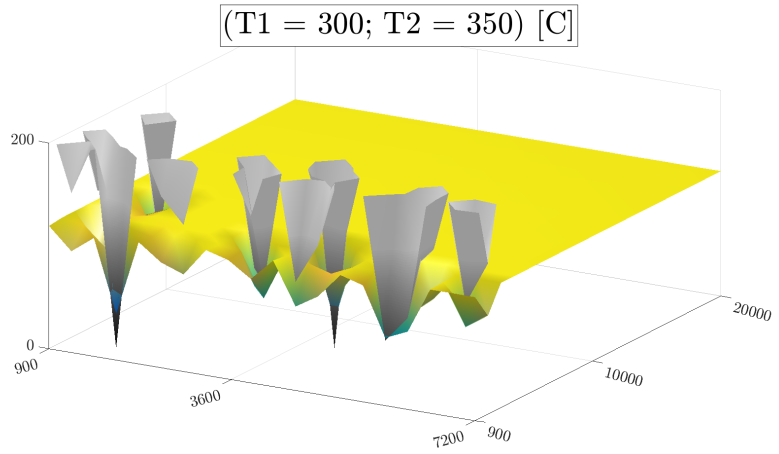

Figure 3.1: Two metrics for the comparison of candidate and target heat treatments. The yellow surface represents the distribution comparison derived fitness surface while the gray cones represent the fitness surface of the single-value metric of Ni content of the matrix.

In NiTi systems, one of the most important physical parameters is the concentration of Nickel in the matrix, which can change the transformation temperature of the material by over 300 degrees with a change of only 1.5at%Ni [56]. The grayscale surface in Figure 3.1 represents the difference in martensitic start temperature for each candidate heat treatment which is calculated based on the difference in Ni-content of the candidate and target matrix phases as described in Tang [56]. The color surface represents the differences in the PSDs of the candidate and target solutions which were calculated using the comparison techniques described throughout the rest of this section.

The most important takeaway from the comparison of these two metrics in Figure 3.1 is that their minima occur at the same basal locations of the surface plot, meaning that they agree on the times and temperatures of the best heat treatment, thus proving that PSDs capture the same information that single valued metrics.

The correlation between concentration of nickel in the matrix and volume fraction transformed is nothing new, but the PSD comparison's reproduction of that exact phenomenon with no prior "knowledge" is what makes such a strong argument for using a PSD as a system descriptor.

3.2 Techniques for Comparing Distributions

Now that distributions have been established as the comparison metric, a technique for comparing them must be developed. Two common distribution comparison techniques are the Kolmogorov-Smirnov (KS) and Chi-Squared (CS) tests, which are typically used to compare distributions of continuous and discrete variables, respectively [33, 45]. This section describes these two techniques, then explains the pros and cons of each before developing a unique approach that combines elements from both to minimize their disadvantages.

3.2.1 The Kolmogorov-Smirnov Test

In short, the KS test converts the candidate and target PSDs into their respective continuous distribution functions (CDFs), then finds the maximum difference between those CDFs (D_{KS}) as seen in Equation KS fitness.

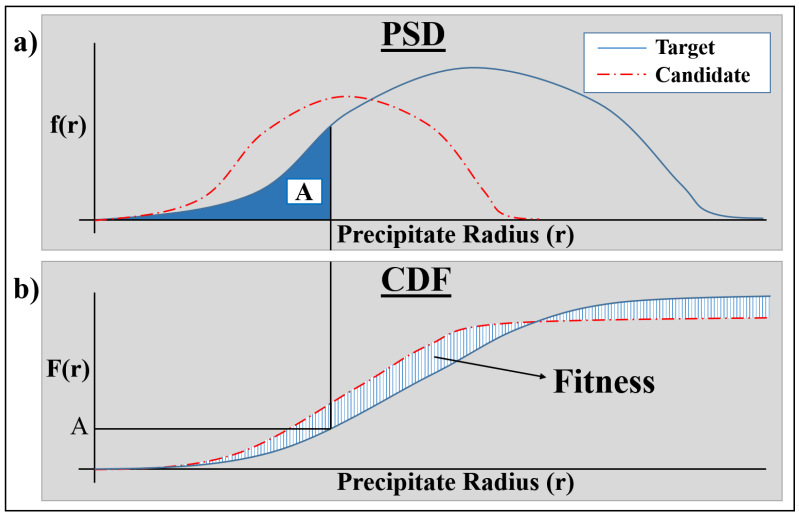

Figure 3.2: Plots of example PSD and CDF equations. The CDF is a function of the total area under the PSD curve up to the corresponding precipitate radius. The fitness metric of any candidate system is the absolute value of the area between the target system CDF and its own.

In the context of this thesis the CDF can be thought of as another way to characterize a distribution F(r) of a system i that represents the total volume of particles with radii smaller than radius r (Figure 3.2b). Three relatively simple mathematical representations of a typical CDF are listed in (Table CDF).

Table 3.1: Different approximation equations that could be used to describe a Continuous Distribution Function seen in Figure 3.2b.

CDF Type	CDF Equation
continuous	$F(r) = \int_0^r f(r)dr'$
step	$\bar{F}(r) = \sum_{i=0}^{r} \bar{f}(i)$
trapezoid	$\tilde{F}(r) = \sum_{i=1}^{r} \frac{\tilde{f}(i)-\tilde{f}(i-1)}{2}(r_i - r_{i-1})$

All three equations use the radii and number of precipitates in each bin as data points for calculating the functions $\mathrm{f(r)}, \bar{\mathrm{f}}\mathrm{(r)}, \tilde{\mathrm{f}}\mathrm{(r)}$. Although the continuous function f(r) represents the most exact representation, determining a function that fits those data points and performing an analytical integration F(r) is too computationally expensive to be feasible in the context of this research, especially when considering the dramatic shapes of some of the distributions. Therefore, each PSD is approximated with either a step function $\bar{\mathrm{f}}\mathrm{(r)}$ or a linear piecewise function $\tilde{\mathrm{f}}\mathrm{(r)}$.

3.2.2 The Chi-Squared Test

In contrast to the KS test, the CS test simply adds the total normalized difference between corresponding bins directly from the target and candidate PSDs as seen in Equation CS fitness [45].

$$D_{CS} = \sum_{i=1}^{r_{max}} \frac{(f_T - f_C)^2}{f_T} \tag{3.1}$$

3.2.3 Analysis of KS and CS Techniques

In research and industry, the KS and CS techniques are typically used to characterize PSDs of industrial powders and soil samples [60, 59, 21, 30, 22]. For example,

soil sample radii are typically classified into different sizes with sieves (discretized), but industrial powders are often classified on a particle-by-particle basis from micrograph image analysis (continuous). Even though the underlying variable is continuous in both scenarios, either discrete and continuous distribution test can be used because it is the type of data resulting from the particle classification process that determines the analysis technique.

3.3 Combined Distribution Comparison Technique

There are drawbacks to each test however: the KS test places too much emphasis on the difference between inflection points of each CDF and the CS test is limited to distribution comparisons with lined up bins [45]. The hybrid approach, created during this research, compensates for both of these shortcomings by combining elements from both techniques. From the KS test, the conversion from PSD to CDF is used to ensure non-zero values and, from the CS test, the bin-by-bin comparison technique is used to spread the emphasis out over the entire combined range of the two CDFs. The differences between the candidate and target CDFs are calculated at 500 regularly spaced intervals over their combined range. The fitness of the candidate solution is calculated with Equation 3.3 which uses the vertical differences and interval spacing to trapezoidally approximate the total area between the CDFs (Figure 3.2b).

$$D_A = \sum_{i=1}^{r_{max}} \left| \frac{r_i - r_{i-1}}{4} \sum_{j=1}^{i} \left[(r_j - r_{j-1})(\Delta\tilde{f}_j + \Delta\tilde{f}_{j-1}) \right] + ... \right.$$
$$\left. ... \sum_{j=1}^{i-1} \left[(r_j - r_{j-1})(\Delta\tilde{f}_j + \Delta\tilde{f}_{j-1}) \right] \right| \tag{3.2}$$
$$Where : \Delta\tilde{f}_j = \tilde{f}_{Cj} - \tilde{f}_{Tj}$$

In order to visualize the fitness space created by Equation 3.3, an array of surface and/or contour plots (Figure 3.3) can be created by evaluating the fitness of a sufficiently large number of candidate solutions. In this array, which is essentially a two dimensional grid of three dimensional plots, each individual contour plot represents the fitness landscape resulting from a parametric sweep of the primary and secondary treatment temperatures while holding their respective treatment times at constant values which are indicated in the title of each plot. As an analogy, each plot in Figure 3.3 can be thought of as a 3D slice of a 5D solution space, just like a single MRI image is a 2D slice of a 3D space. Once enough slices are imaged, a much more comprehensive picture of the space can be formed. the through the fitness space at certain times.

Therefore, each point on the surfaces and/or contour plots represents the fitness of one candidate solution whose 2 time and 2 temperature values can be determined based on: i) the (x,y) location of the plot it is inside, ii) its (x,y) location inside of that plot, respectively. The black lines on the contour plots depict the two temperatures of the target heat treatment (550 °C and 250 °C) meaning that the contour plot which has a minimum located nearest to the intersection of the two black lines is the fittest individual in the array of plots. For example, in Figure 3.3, the minimum point in the lower right contour plot is closest to the target temperature intersection and corresponds to the heat treatment vector [251, 3000, 551, 20000].

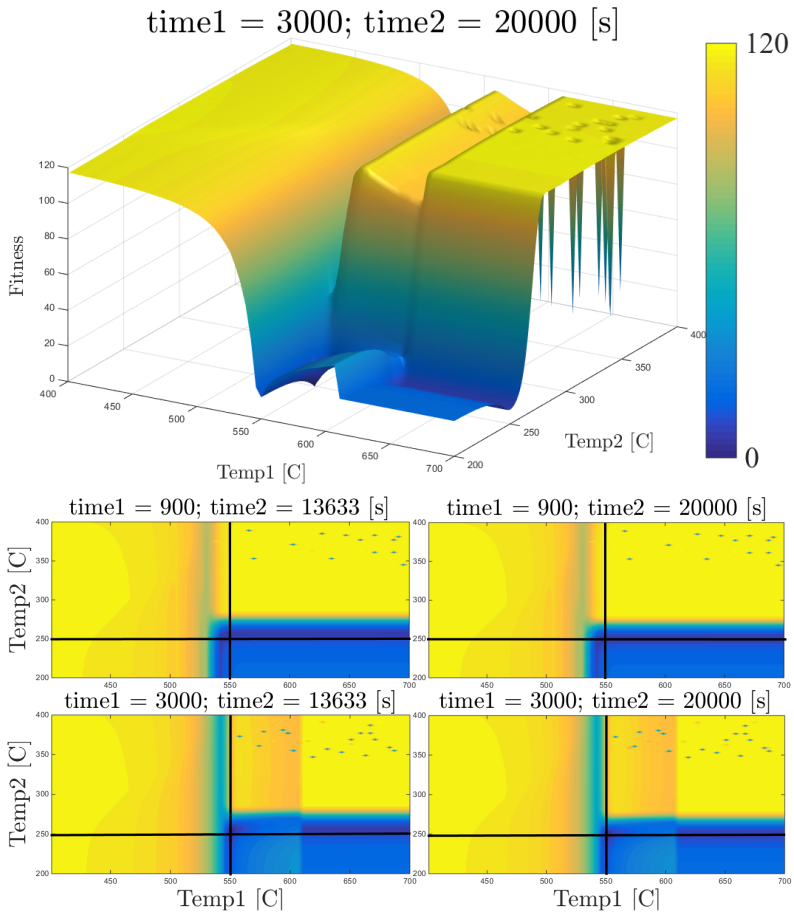

Figure 3.3: A 2 dimensional array of 3 dimensional slices representing the 5 dimensional search space. Note the proximity of each minimum to the target times and temperatures of 250[C] and 550[C].

The simulation and fitness calculation at each surface point is reasonably quick (1 minute), but the sheer number of calculations necessary to consistently capture the global minima pushes the overall calculation time to unreasonably large values. These surfaces are still incredibly useful at lower resolutions as visual representations of general trends and rough validation of optimization outputs, a topic which will be discussed in the next section.

4. SEARCHING THE SOLUTION SPACE

An analogy showing the differences between gradient and non-gradient based approaches is given at the beginning of this section. The rest of the section is a discussion of the theories underlying Mesh Adaptive Direct Search, which is the optimization technique utilized in this research.

4.1 Gradient Based vs. Non-Gradient Based Optimization

The best physical analogy of the differences between gradient and non-gradient based optimization can be thought of in the context of a situation in which someone has been tasked with finding the lowest point in a swimming pool filled with water. The simplest physical analog to a gradient based approach would be to drop a steel ball in the pool and record where it comes to rest. In this situation, gravity is the driving force that pulls the ball down the steepest gradient possible until the ball reaches some equilibrium value (i.e. gradient is zero), which is then assumed to be the lowest point in the pool.

Now that the gradient based approach has been solved, an interesting question to ask is, what would a feasible approach to this problem be if there are not any balls that sink in water? The physical limitation of not having a ball is analogous to the mathematical limitations of not having gradient information about a solution space. One physical technique for finding the lowest point would be to grab a kayak and float around the pool while using a stick to measure the depth of the water. It's very unlikely that this technique will find the lowest point in the pool within the first few measurements, but as more and more depths are recorded, the lowest point in the pool will eventually be found.

So far, this non-gradient approach has been framed as a random search, but

it should be fairly obvious that a more systematic approach to sampling points would lead to faster convergence to the solution. If information about previous measurements is taken into consideration when selecting new measurement points the area in which guesses are made should decrease and the point where this search area shrinks to some reasonable size is considered the lowest point in the pool.

4.2 Definition of Search Space

The optimizations conducted in this research follow the same logic as the systematic non-gradient approach described in the section above, but instead of a 3 dimensional search space (pool location and depth), they must deal with a 5 dimensional solution space. The first 4 dimensions of the search space consist of 2 times and 2 temperatures that describe the candidate heat treatment (pool location), followed by a 5th dimension describing the fitness of the candidate (pool depth). A schematic of a generic two stage heat treatment illustrating the time and temperature dimensions mentioned above can be seen in Figure 4.1.

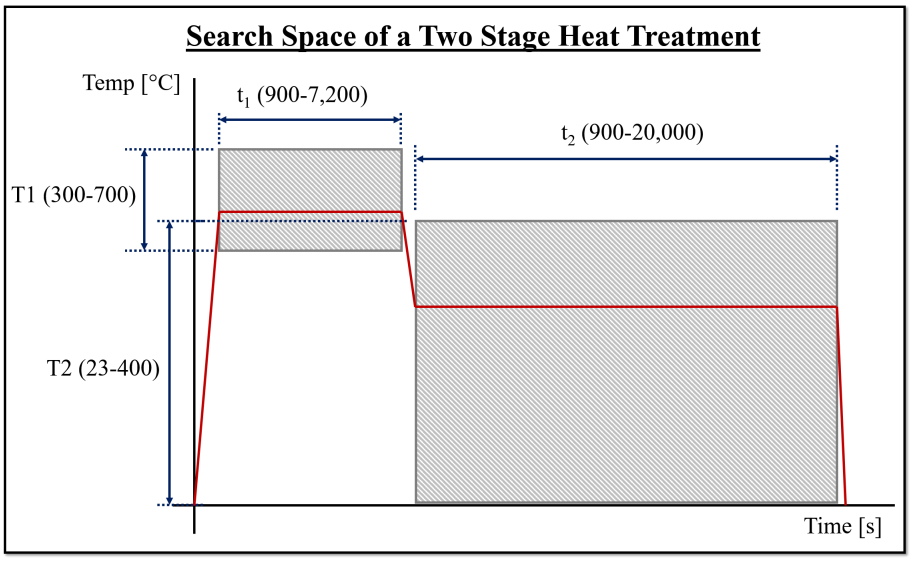

Figure 4.1: Schematic heat treatment showing the searchable dimensions in a two stage heat treatment. The search space is bounded by the ranges of the 2 times and 2 temperatures listed in the diagram.

As seen in Figure 3.3 from Section 3.3, the large changes in fitness and number of local minima make it clear that finding the relative global minimum using brute force search techniques would require an unrealistically fine resolution. Instead, an optimization tool is used to efficiently search the space for the location (described by the vector [t_1, T_1, t_2, T_2]) of the relative global minimum of the 5 dimensional solution space.

4.3 NOMAD Optimization

NOMAD [1] was selected for its lack of reliance on the derivative of the fitness function and its ability to integrate with black box style programs like the Python-based MatCalc interface used during this research [32, 7, 4]. For a more comprehensive look at the flow of information between NOMAD and the MatCalc interface, the reader is referred to the optimization flowchart in (Figure 4.2).

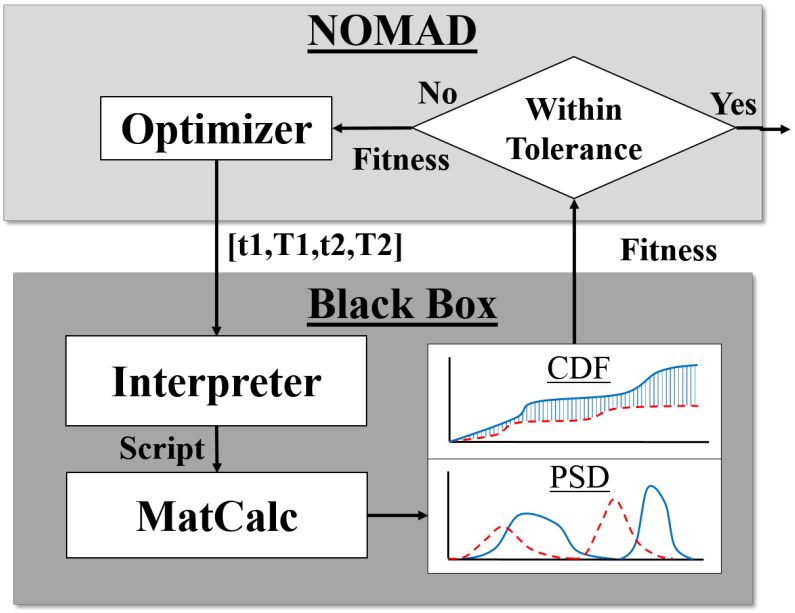

Figure 4.2: Flowchart depicting the flow of information in the prescriptive heat treatment framework.

4.3.1 Mesh Adaptive Direct Search

NOMAD uses a mesh adaptive direct search (MADS) algorithm; a pattern search technique that seeks to increases fitness at each iteration by performing search and poll steps at each iteration [32, 4]. The search step consists of evaluating the fitness of a set of trial points selected randomly from a mesh which surrounds the incumbent solution and also includes previous most fit solutions from past iterations [5]. If no trial points are more fit than the incumbent solution, the poll step is initiated which is essentially a more localized and refined set of trial points selected from a mesh which is built from linear combinations of randomly generated pattern basis vectors that span the solution space. The number of pattern basis vectors is typically either 2N or N+1 where N is the number of variables in the search space. The mesh can either increase or decrease its spacing in response to the evolution of fitness from past

iterations, as well as the results of the search and poll steps of the current iteration.

The combination of mesh refinement and randomly generated poll directions, is the key feature that distinguishes MADS from other pattern search techniques like generalized pattern search (GPS). This decouples the mesh and poll size parameters so the trial points are not limited to a finite number of directions, which is the limiting factor in GPS approaches. For example, in a two dimensional search grid, a 2N GPS algorithm will always use pattern basis vectors that are orthogonal to the solution variables (i.e. v_1,v_3=[$\pm 1, 0$], v_2,v_4=[$\pm 1, 0$]), but MADS will randomly generate pattern basis vectors that are not necessarily vertical or horizontal, allowing for a more comprehensive search of the solution space [5]. The chance that the algorithm will miss the optimal solution can be decreased even further by using the OrthoMADS search scheme in NOMAD [2]. This search scheme minimizes the cosine measure of the pattern basis vectors ($1/\sqrt{\mathrm{N}}$) by adding the additional constraint that they must be orthogonal to each other, but still not necessarily orthogonal to the search space variables [2].

4.3.2 Escaping Local Minima

The issue of local minima trapping plagues many optimization techniques including OrthoMADS. Fortunately, NOMAD helps alleviate this issue by providing tools like variable neighborhood search (VNS) which significantly expands the scanning area of the search step in each iteration allowing the algorithm to escape local minima [7, 6]. The VNS search is controlled by two parameters that specify the distance with which to perturb the system (updated at each iteration) and how long to search for the optimum solution at that perturbed neighbor [19, 4, 37].

NOMAD also includes latin hypercube sampling (LH), which is another useful search technique that creates a family of trial points by evenly splitting the domains of

each input variable and selecting one random number from a section in each variable until one value from every section of every variable has been used [55, 52, 34]. The LH method of trial point selection is more efficient at spanning the entire domain of a variable than a simple random search method. The drawback of these methods is that they increase the overall calculation time of the optimization. The fitness landscape of every optimization problem is unique and OrthoMADS with VNS and LH search techniques may not be the best algorithm choice.

Although outside the scope of this research, genetic optimization techniques also have proven track records of escaping local minima and may be well suited to a variety of optimization frameworks in this area [10, 17, 65, 65]. A brief discussion of genetic optimization techniques as a future direction of this research is included in the conclusion of this thesis.

5. SUMMARY OF PREDICTION FRAMEWORK

With the conclusion of this section, every component of the predictive framework necessary to link structure to processing from the top down has been developed. Governing equations for nucleation, growth, and coarsening were derived and combined into a comprehensive material model which was then calibrated using an experimental heat treatment that resulted in a bimodal precipitate size distribution. Then a technique for comparing distributions of candidate heat treatments to that of a target heat treatment was developed by combining elements of the KS and CS statistical tests. Finally, the material model and comparison technique were combined with an optimization technique which uses Mesh Adaptive Direct Search to efficiently search the solution space for a heat treatment which results in the same distribution as that of the target solution. This predictive framework must now be tested to determine its effectiveness and Section 6 focuses on the results of these prediction efforts.

6. RESULTS

6.1 Calculation of Target Distribution

Now that the kinetic model has been calibrated, a fitness metric has been established, and both of those features have been integrated with the NOMAD optimization environment, the next step is to see if the framework can successfully prescribe a heat treatment that results in a predefined target precipitate size distribution.

To showcase the versatility of this approach/framework, MatCalc was used to produce a theoretical PSD based on a two-stage heat treatment from the literature that resulted in a multimodal PSD [66]. This multimodal system is an excellent candidate for the framework presented in this model because it showcases the type of complex yet practical microstructures that it can handle. The precipitates with larger radii, used to tailor matrix Ni content and to create coherent stress fields, are created by a 1 hour high temperature heat treatment at 550 °C. The precipitates with smaller radii, also used to tailor matrix Ni content and to inhibit dislocation motion, are created by holding at an aging temperature of 250 °C for 5 hours. According to Zeldovich, the larger particles ranged in diameter from 0.2-0.8 μm while the smaller particles were described as roughly two orders of magnitude smaller. As discussed in Section 4.2 this two stage heat treatment is described by the vector [3600, 550, 18000, 250] which list the temperatures and times of the two treatments as such: [time 1, Temperature 1, time 2, Temperature 2]. The MatCalc calculated volume PSD and subsequent CDF for this target heat treatment can be seen in Figure 6.1 where the distributions and fitnesses of one unfit and one fit candidate are compared to those of the target system ((a & b) and (c & d), respectively) .

UNFIT CANDIDATE	FIT CANDIDATE
$[T_1 = 550[C], t_1 = 2000[s],$ $T_2 = 270[C], t_2 = 10000[s]]$	$[T_1 = 550[C], t_1 = 5383[s],$ $T_2 = 72[C], t_2 = 4009[s]]$
a) 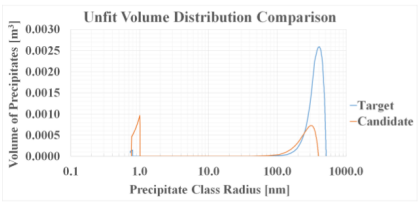	b) 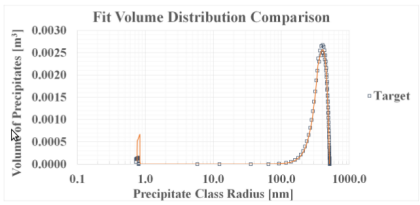
c) 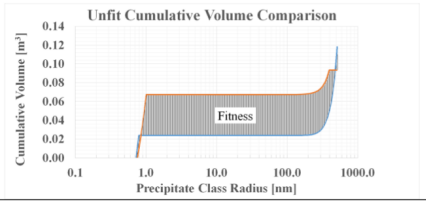	d) 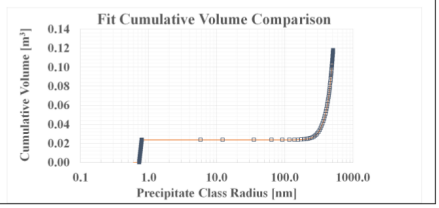

Figure 6.1: Comparison of two Ni_4Ti_3 PSDs and corresponding CDFs for one fit and one unfit candidate heat treatment. The heat treatment vectors for each candidate can be seen at the top of the their respective columns. The target system is described by the heat treatment vector: **[T1=550[C], t1=3600[s], T2=250[C], t2=18000[s]]**

6.2 Predicting Target Heat Treatment

6.2.1 Defining the Search Space

After the target system's PSD is calculated, the vector of target temperatures and times outlined in the previous paragraph is "forgotten" so that the only information about the target available to the prescriptive framework are the PSD and nominal composition. This means that this target distribution can be treated as if it came from experimental data and therefore used to simulate a scenario in which a scientist needs to determine the heat treatment history of a particular sample with limited prior knowledge. The only two assumptions necessary to establish reasonable limits on the search space are i) a fairly obvious assumption that the bimodality of the target distribution is the result of a two stage heat treatment (to establish the number of

necessary HT variables) and ii) basic knowledge of the thermodynamics of the system (to establish the temperature and time ranges of each variable). Wide but reasonable temperature and time ranges (see Table 6.1) were selected for the search space to complete the theme of limited prior knowledge.

Table 6.1: Limits on the times and temperatures listed in the candidate heat treatment vector.

Variable	Range
T1	$200 - 400[^{\circ}C]$
t1	$900 - 7200[s]$
T2	$300 - 700[^{\circ}C]$
t2	$900 - 20000[s]$

6.2.2 Predicted Heat Treatments

The search space limits (Table 6.1) and material framework are provided to NOMAD and its convergence limits were systematically lowered to determine the tolerance threshold necessary to accurately prescribe heat treatments. A few NOMAD prescribed heat treatments have been plotted in Figure 6.2 to show trends in the predicted times and temperatures as the heat treatments become more and more fit. The first stage is almost perfectly prescribed by each optimization but the second stage needs much tighter tolerances to accurately predict its temperature and time. Although the prescribed times and temperatures seem quite sporadic, an inverse relationship between temperature and time with respect to fitness is readily apparent in the inset of Figure 6.2. This means that, as the optimization tolerances are tight-

ened, the prescribed secondary heat treatment times should continue to converge to their respective target values.

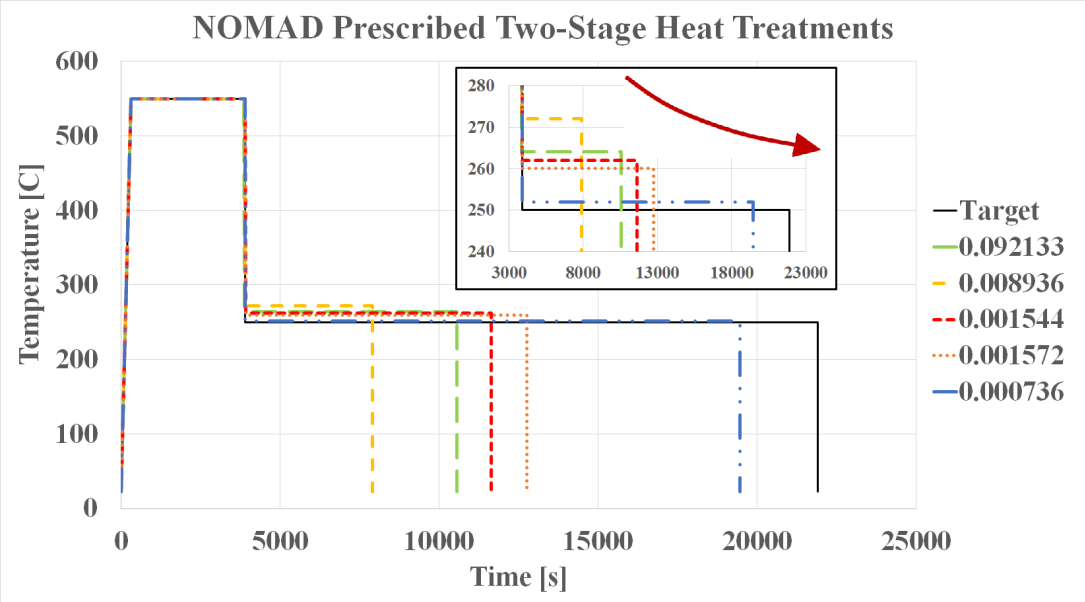

Figure 6.2: Examples of heat treatment candidate solutions prescribed by the framework developed in this text. The heat treatments are labeled with their calculated fitness values. The inset shows a detailed view of the second stages of the prescribed heat treatments. Note the trend of longer times and lower temperatures with an increase in fitness.

6.2.3 Convergence Analysis

Candidate heat treatments and their corresponding fitness values were tracked over the course of the entire NOMAD optimization for a few of the predicted heat treatments shown in Figure 6.2 to analyze the effectiveness of Latin Hypercube and Variable Neighborhood Search parameters. Three cases can be seen below in Figures 6.3, 6.4, and 6.5.

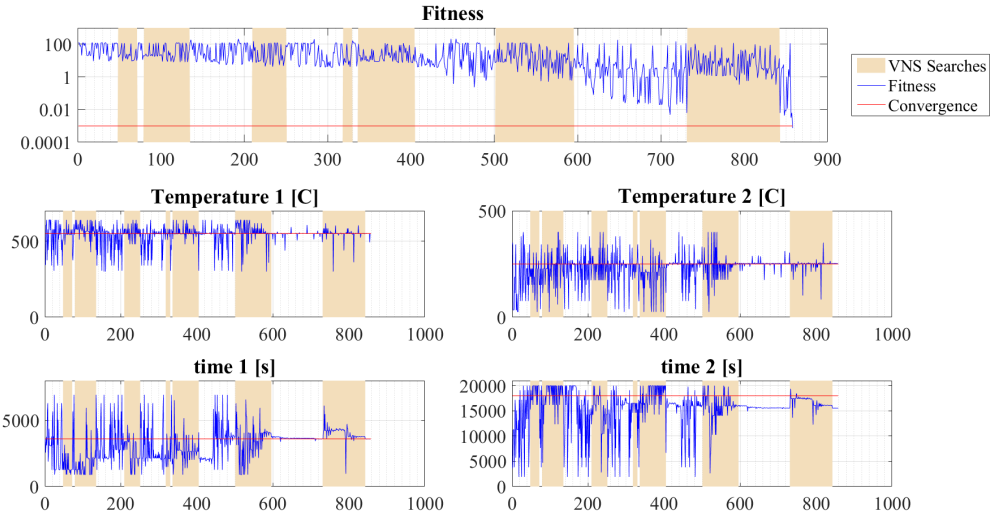

Figure 6.3: Heat treatment times and temperatures, and their corresponding fitness values over the course of a NOMAD optimization with a 40%VNS and 200 initial/5 step LH search parameters. Note that Variable Neighborhood Searches, highlighted with an orange background, do not necessarily move the solution in the direction of the global minimum.

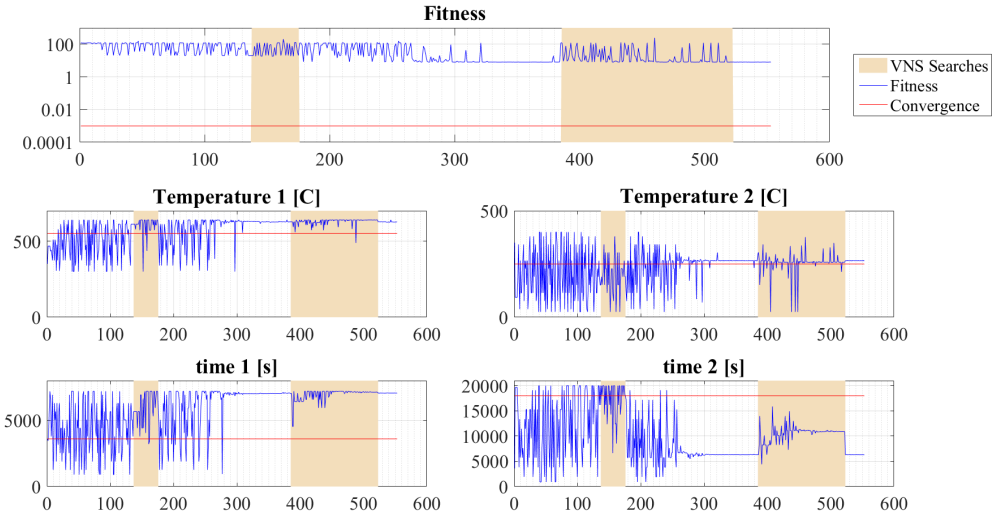

Figure 6.4: Heat treatment times and temperatures, and their corresponding fitness values over the course of a NOMAD optimization with 10%VNS searches and 200/5 LH search parameters. Note that Variable Neighborhood Searches, highlighted with an orange background, do not necessarily move the solution in the direction of the global minimum.

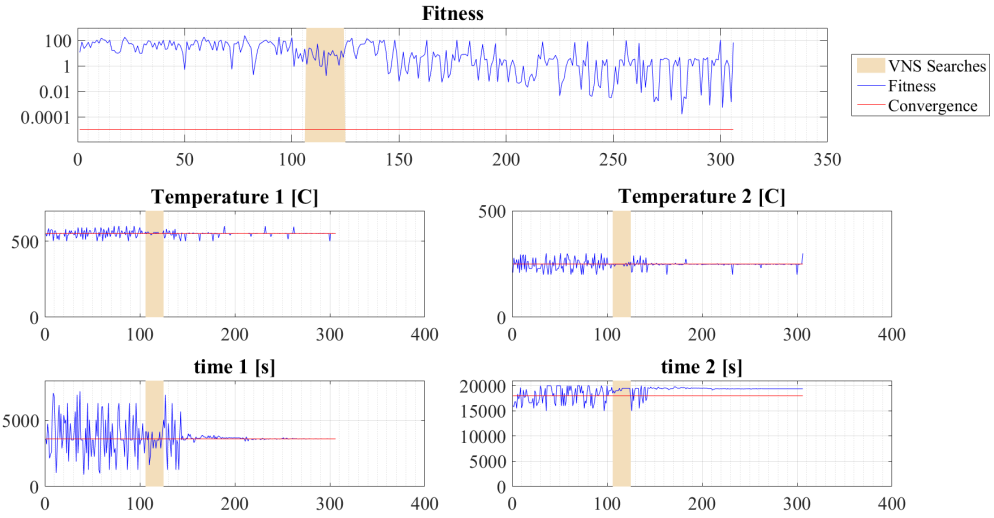

Figure 6.5: Heat treatment times and temperatures, and their corresponding fitness values over the course of a NOMAD optimization with a 5%VNS and 200 initial/5 step LH search parameters. Note that Variable Neighborhood Searches, highlighted with an orange background, do not necessarily move the solution in the direction of the global minimum.

Obviously there are times when VNS helps escape local minima and there are times when VNS leads the solution away from the global minimum, but it seems like it leads the optimizer astray more often than not. The effectiveness of the Latin Hypercube search on any one run is harder to see because of it's fundamental basis in system wide randomness. Analysis of the effectiveness of both of these tools, along with many other tools used in this framework, is presented in the following conclusion section.

7. CONCLUSIONS

The concepts underlying this framework were tested using a 52.0 at% Ni system with a target bimodal distribution brought about by a two stage heat treatment. Through the course of this research, a computational framework was developed that can predict the heat treatment of a NiTi shape memory alloy that will result in a desired precipitate size distribution. This top-down relationship between structure and processing i the last link in the goal driven materials design scheme that allows material development to be directly integrated into the iterative design process of engineering project as a whole. The framework consists of its own iterative optimization process that incorporates a kinetic model and a distribution comparison technique with a mesh adaptive direct search tool to find a heat treatment that results in a desired precipitate size distribution.

7.1 Precipitation Modeling

The parameters of the precipitation model are currently calibrated against a small number of systems, which means the model has a fairly narrow range of times and temperatures that it can accurately predict the precipitate size distribution, increasing the chance that the target heat treatment may not be included in the search space. To combat this, current research introduces a temperature dependent factor to some of the parameters including a matrix diffusion enhancement coefficient that modifies the kinetic values provided in MatCalc's databases. Additionally, collaborations have been established with Dr. Elwany in the Industrial Engineering Department at Texas A&M University to calibrate the parameters of this precipitation model using Bayesian statistical analysis based on martensitic transformation temperatures taken from Brian Franco's thesis work.

Another area that can be expanded upon here is the complexity of the precipitation model used in this paper. As discussed in the material selection section above, external stress has a significant effect on the morphology of precipitates in the system, a fact which has not been considered in the research of this thesis, but could be introduced to the precipitation model as either another variable to predict, or as a known quantity based on a desired experimental test. Other key microstructural features can be described via distributions and/or contour maps (grain size, orientational pole figures, etc.) which can be analyzed using the same comparison techniques presented in this paper. MatCalc does not simulate orientation evolution but it does contain some governing equations that predict the evolution of microstructural features such as grain size and dislocation density in response to external stresses as well as aging treatments. This would allow for the prediction of thermo-*mechanical* processing steps.

7.2 Distribution Comparison

The statistical test used to compare target and candidate solutions in this framework is a combination of Chi-Squared and Kolmogorov-Smirnov statistical tests. This spreads the comparison out evenly over the entire range of both distributions and behaves well in the presence of zero-valued bins. The transition from comparisons of single valued metrics to comparisons of distributions significantly reduced the degeneracy of the solution and lead to more physically appropriate, but even more factors such as production cost (as a function of time, temperature, and composition) can be added to the fitness metric of each candidate in order to reduce the degeneracy even further. After including industrially relevant modifications to the fitness function such and time and temperature penalties, the next step will be to relax the assumptions used to create the initial search space (i.e. limit 'prior knowl-

edge' even further), increasing the dimensionality of the search space which leads to a more powerful prediction tool.

7.3 Search Technique

The search technique in this prediction framework is the section with the most room for improvement. This research presented a set of predicted heat treatments that fell within convergence tolerances (Figure 6.2), but there were a significant number of optimization trails in which the NOMAD search algorithm became trapped in a local minimum. While complex fitness surfaces with steep transition regions and multiple local minima are perfect examples of what the Latin Hypercube and Variable Neighborhood Search modifications in NOMAD are design to deal with, lack of flexibility in these module's parameters made it difficult to tailor them for consistent convergence to the global minimum. For example, the only parameter available for tuning the VNS module is a single value dictating the fraction of total optimization searches that should be VNS based. The Latin Hypercube implementation has a little bit more flexibility in the sense that there are two parameters which let the user define the number of LH searches at the initial search step and at every other step thereafter.

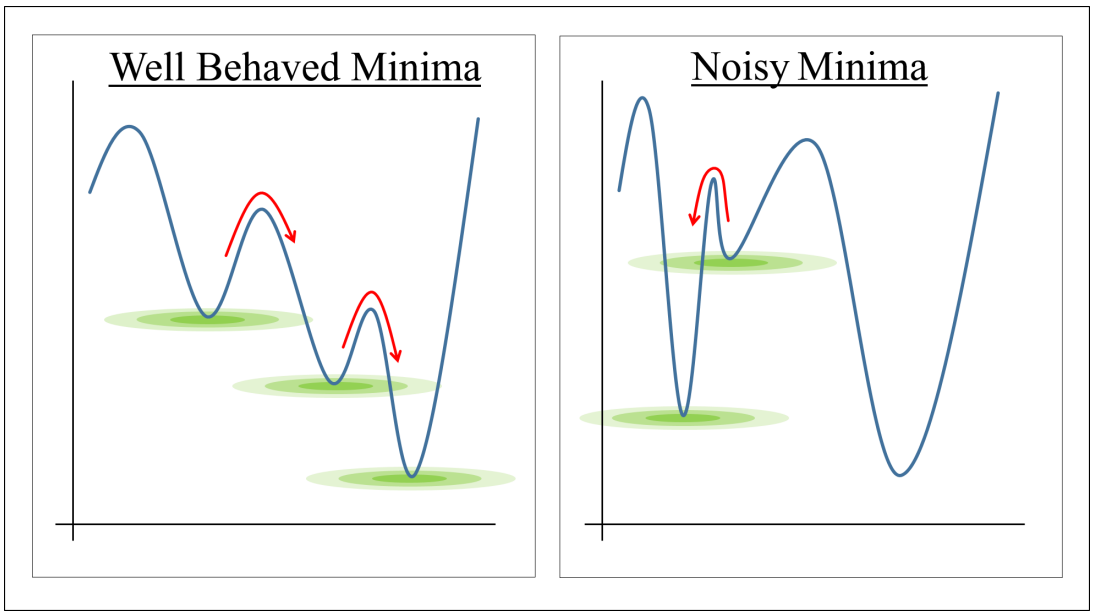

Figure 7.1: Comparing VNS search strategies between search spaces with different local minima landscapes. The minima values on the left tend to approach global minimum values while the ones on the left do not, leading to convergence to local minima trapping.

VNS may not be the best way to escape the local minima landscape of this particular solution space. One fundamental assumption underlying the viability of VNS is that the local minima values of the search space will generally trend toward values approaching the global minimum. This assumption does not necessarily hold and Figure 7.1 compares two theoretical cases; one in which VNS makes sense and one in which it does not. These issues can be dealt with by changing parameters that control VNS search behavior such as threshold values for local minima identification and minima hopping criteria, but NOMAD does not allow for the modification of these factors.

The prediction of viable heat treatments using the overall framework presented in this thesis validates the framework's underlying concepts, but there may be op-

timization based search tools better suited for this design framework and fitness landscapes like the one seen in Figure 3.3. Genetic Algorithms are a class of search tools which are well known for being able to escape local minima, but they typically take more iterations to converge. That being said, it is important to point out that there is no magic bullet for optimization and the fitness landscape of each solution space should be considered on a case-by-case basis to determine the best approach.

7.4 Overall Summary

At its simplest, the framework is a three part system which consists of a precipitation model, a statistical comparison technique, and an optimization tool used to sample the search space. Although the framework as it stands now correctly predicted the two stage heat treatment, there is room for improvement in each of its three main sections. Therein lies the power of this type of design framework: any type of model or analytical tool can be used in its appropriate section, as long as the three main parts of the system have a way to interface with one another. This section has detailed potential areas for future expansion and refinement including model abstractions and entirely different analytical techniques for each of the three main components of the overall predictive framework. It is important to note that although heat treatments of a NiTi SMA was used to prove the veracity of this framework, there is nothing limiting this framework to that particular material system. This means that the framework presented in this thesis can predict the heat treatment history of any material system that contains precipitates with a well calibrated kinetic precipitation model.

REFERENCES

[1] M. Abramson, C. Audet, G. Couture, J. Dennis, Jr., S. Le Digabel, and C. Tribes. The NOMAD project. *Software available at https://www.gerad.ca/nomad/.*

[2] M. Abramson, C. Audet, J. Dennis, and S. Digabel. Orthomads: A deterministic mads instance with orthogonal directions. *SIAM Journal on Optimization*, 20(2):948–966, Jan. 2009.

[3] J. K. Allafi, X. Ren, and G. Eggeler. The mechanism of multistage martensitic transformations in aged Ni-rich NiTi shape memory alloys. *Acta Materialia*, 50(4):793–803, 2002.

[4] C. Audet, V. Bchard, and S. L. Digabel. Nonsmooth optimization through mesh adaptive direct search and variable neighborhood search. *Journal of Global Optimization*, 41(2):299–318, Oct. 2007.

[5] C. Audet and J. Dennis. Mesh adaptive direct search algorithms for constrained optimization. *SIAM Journal on Optimization*, 17(1):188–217, Jan. 2006.

[6] C. Audet, J. E. Dennis Jr, and S. Le Digabel. Globalization strategies for mesh adaptive direct search. *Computational Optimization and Applications*, 46(2):193–215, 2010.

[7] C. Audet, S. Le Digabel, and C. Tribes. NOMAD user guide. Technical report, Les cahiers du GERAD, Montreal, Quebec, 2009.

[8] L. Bataillard, J.-E. Bidaux, and R. Gotthardt. Interaction between microstructure and multiple-step transformation in binary NiTi alloys using in-situ trans-

mission electron microscopy observations. *Philosophical Magazine A*, 78(2):327–344, 1998.

[9] T. Baxevanis, A. Cox, and D. Lagoudas. Micromechanics of precipitated near-equiatomic Ni-rich NiTi shape memory alloys. *Acta Mechanica*, 225(4-5):1167–1185, 2014.

[10] A. P. A. Borisovsky, XavierDolgui. Genetic algorithm for balancing reconfigurable machining lines. *Computers & Industrial Engineering*, 66(3):541–547, Nov. 2013.

[11] J. W. Christian. *The Theory of Transformations in Metals and Alloys*. Newnes, Kidlington, Oxford, 2002.

[12] J. Eshelby. The determination of the elastic field of an ellipsoidal inclusion, and related problems. *Royal Society of London Proceedings Series A*, 241:376–396, 1957.

[13] G. Fan, W. Chen, S. Yang, J. Zhu, X. Ren, and K. Otsuka. Origin of abnormal multi-stage martensitic transformation behavior in aged Ni-rich Ti–Ni shape memory alloys. *Acta Materialia*, 52(14):4351–4362, 2004.

[14] J. Feder, K. Russell, J. Lothe, and G. Pound. Homogeneous nucleation and growth of droplets in vapours. *Advances in Physics*, 15(57):111–178, 1966.

[15] J. Frenzel, E. P. George, A. Dlouhy, C. Somsen, M.-X. Wagner, and G. Eggeler. Influence of Ni on martensitic phase transformations in NiTi shape memory alloys. *Acta Materialia*, 58(9):3444–3458, 2010.

[16] D. T. Fullwood, S. R. Niezgoda, B. L. Adams, and S. R. Kalidindi. Microstructure sensitive design for performance optimization. *Progress in Materials Science*, 55(6):477–562, 2010.

[17] A. Garg, L. Rachmawati, and K. Tai. Classification-driven model selection approach of genetic programming in modelling of turning process. *The International Journal of Advanced Manufacturing Technology*, 69(5-8):1137–1151, June 2013.

[18] J.-H. Ha, S. K. Kim, N. Cohenca, and H.-C. Kim. Effect of R-phase heat treatment on torsional resistance and cyclic fatigue fracture. *Journal of Endodontics*, 39(3):389–393, 2013.

[19] P. Hansen and N. Mladenovi. Variable neighborhood search: Principles and applications. *European Journal of Operational Research*, 130(3):449–467, May 2001.

[20] I. Holzer, E. Kozeschnik, and H. Cerjak. New approach to predict the long-term creep behaviour and evolution of precipitate back-stress of 9–12% chromium steels. *Transactions of the Indian Institute of Metals*, 63(2-3):137–143, 2010.

[21] C. Igathinathane, U. Ulusoy, and L. O. Pordesimo. Comparison of particle size distribution of celestite mineral by machine vision volume approach and mechanical sieving. *Powder Technology*, 215216:137–146, Jan. 2012.

[22] J. L. H. Jr. The significance probability of the Smirnov two-sample test. *Arkiv fr Matematik*, 3(5):469–486, Jan. 1958.

[23] J. Khalil-Allafi, A. Dlouhy, and G. Eggeler. Ni4Ti3-precipitation during aging of NiTi shape memory alloys and its influence on martensitic phase transformations. *Acta Materialia*, 50(17):4255–4274.

[24] J. Khalil-Allafi, G. Eggeler, A. Dlouhy, W. W. Schmahl, and C. Somsen. On the influence of heterogeneous precipitation on martensitic transformations in

a Ni-rich NiTi shape memory alloy. *Materials Science and Engineering: A*, 378(1):148–151.

[25] J. I. Kim and S. Miyazaki. Effect of nano-scaled precipitates on shape memory behavior of Ti-50.9at.%Ni alloy. *Acta Materialia*, 53(17):4545–4554.

[26] M. Kohl, D. Dittmann, E. Quandt, and B. Winzek. Thin film shape memory microvalves with adjustable operation temperature. *Sensors and Actuators A: Physical*, 83(1):214–219, 2000.

[27] E. Kozeschnik and B. Buchmayr. MATCALC- a simulation tool for multicomponent thermodynamics, diffusion and phase transformations. In *Fifth International Seminar on the Numerical Analysis of Weldability*, pages 349–361, 1999.

[28] E. Kozeschnik, K. Janssens, and C. Bataille. *Modeling solid-state precipitation*. Momentum Press, New York City, New York, 2012.

[29] E. Kozeschnik, J. Svoboda, and F. Fischer. Modified evolution equations for the precipitation kinetics of complex phases in multi-component systems. *Calphad*, 28(4):379–382, 2004.

[30] F. Lampariello. On the use of the Kolmogorov-Smirnov statistical test for immunofluorescence histogram comparison. *Cytometry*, 39(3):179–188, Mar. 2000.

[31] J. Langer and k. Schwartz. Kinetics of nucleation in near-critical fluids. *Physical Review A*, 21(3):948, 1980.

[32] S. Le Digabel. Algorithm 909: NOMAD: Nonlinear optimization with the MADS algorithm. *ACM Transactions on Mathematical Software*, 37(4):1–15, 2011.

[33] F. J. Massey Jr. The kolmogorov-smirnov test for goodness of fit. *Journal of the American Statistical Association*, 46(253):68–78, 1951.

[34] M. D. McKay, R. J. Beckman, and W. J. Conover. Comparison of three methods for selecting values of input variables in the analysis of output from a computer code. *Technometrics*, 21(2):239–245, 1979.

[35] J. Michutta, M. C. Carroll, A. Yawny, C. Somsen, K. Neuking, and G. Eggeler. Martensitic phase transformation in Ni-rich NiTi single crystals with one family of Ni4Ti3 precipitates. *Materials Science and Engineering: A*, 378(1):152–156.

[36] S. Miyazaki and K. Otsuka. Deformation and transition behavior associated with ther-phase in Ti-Ni alloys. *Metallurgical Transactions A*, 17(1):53–63, 1986.

[37] N. Mladenović and P. Hansen. Variable neighborhood search. *Computers & Operations Research*, 24(11):1097–1100, Nov. 1997.

[38] M. Nishida, C. Wayman, and T. Honma. Precipitation processes in near-equiatomic TiNi shape memory alloys. *Metallurgical Transactions A*, 17(9):1505–1515, 1986.

[39] Y. Okamoto, H. Hamanaka, F. Miura, H. Tamura, and H. Horikawa. Reversible changes in yield stress and transformation temperature of a NiTi alloy by alternate heat treatments. *Scripta Metallurgica*, 22(4):517–520, 1988.

[40] G. B. Olson. Computational design of hierarchically structured materials. *Science*, 277(5330):1237–1242, Aug. 1997.

[41] L. Onsager. Reciprocal relations in irreversible processes. i. *Physical Review*, 37(4):405, 1931.

[42] K. Otsuka and X. Ren. Physical metallurgy of TiNi-based shape memory alloys. *Progress in Materials Science*, 50(5):511–678, Jul 2005.

[43] L. Pandelaers, B. Blanpain, and P. Wollants. An optimized diffusion database for the disordered and ordered bcc phases in the binary FeTi system. *Calphad*, 35(4):518–522, Dec 2011.

[44] M. Perez. Gibbs–thomson effects in phase transformations. *Scripta Materialia*, 52(8):709–712, 2005.

[45] F. C. Porter. Testing consistency of two histograms. *arXiv Preprint–arXiv:0804.0380*, 2008. Cornell University.

[46] R. Radis, G. A. Zickler, M. Stockinger, C. Sommitsch, and E. Kozeschnik. Interaction of the precipitation kinetics of δ and γ phases in nickel-base superalloy ATI Allvac 718PlusTM. volume 638, pages 2712–2717. Trans Tech Publ, 2010.

[47] X. Ren, N. Miura, J. Zhang, K. Otsuka, K. Tanaka, M. Koiwa, T. Suzuki, Y. Chumlyakov, and M. Asai. A comparative study of elastic constants of Ti Ni-based alloys prior to martensitic transformation. *Materials Science & Engineering A*, 312:196 – 206, 2001.

[48] X. B. Ren and K. Otsuka. Why does the martensitic transformation temperature strongly depend on composition? volume 327, pages 429–432. Trans Tech Publ, 2000.

[49] J. Robson. Modelling the overlap of nucleation, growth and coarsening during precipitation. *Acta Materialia*, 52(15):4669–4676, 2004.

[50] J. Sietsma and S. van der Zwaag. A concise model for mixed-mode phase transformations in the solid state. *Acta Materialia*, 52(14):4143–4152, 2004.

[51] P. Sittner, M. Landa, P. Lukas, and V. Novak. R-phase transformation phenomena in thermomechanically loaded NiTi polycrystals. *Mechanics of Materials*, 38(5):475–492, 2006.

[52] M. Stein. Large sample properties of simulations using latin hypercube sampling. *Technometrics*, 29(2):143–151, 1987.

[53] J. Svoboda, F. Fischer, P. Fratzl, and E. Kozeschnik. Modelling of kinetics in multi-component multi-phase systems with spherical precipitates: I: Theory. *Materials Science and Engineering: A*, 385(1):166–174, 2004.

[54] J. Svoboda and I. Turek. On diffusion-controlled evolution of closed solid-state thermodynamic systems at constant temperature and pressure. *Philosophical Magazine B*, 64(6):749–759, 1991.

[55] B. Tang. Orthogonal array-based latin hypercubes. *Journal of the American Statistical Association*, 88(424):1392–1397, Dec. 1993.

[56] W. Tang. Thermodynamic study of the low-temperature phase B19' and the martensitic transformation in near-equiatomic Ti-Ni shape memory alloys. *Metallurgical and Materials Transactions A*, 28(3):537–544, 1997.

[57] W. Tirry and D. Schryvers. Quantitative determination of strain fields around Ni 4 Ti 3 precipitates in NiTi. *Acta Materialia*, 53(4):1041–1049, 2005.

[58] W. Tirry and D. Schryvers. Linking a completely three-dimensional nanostrain to a structural transformation eigenstrain. *Nature Materials*, 8(9):752–757, 2009.

[59] D. Van der Weken, M. Nachtegael, and E. Kerre. Using similarity measures for histogram comparison. In *Fuzzy Sets and SystemsIFSA 2003*, pages 396–403. Springer, 2003.

[60] E. Vigneau, C. Loisel, M. F. Devaux, and P. Cantoni. Number of particles for the determination of size distribution from microscopic images. *Powder Technology*, 107(3):243–250, Feb. 2000.

[61] P. W. Voorhees. The theory of Ostwald ripening. *Journal of Statistical Physics*, 38(1-2):231–252, 1985.

[62] R. Wagner, R. Kampmann, and P. W. Voorhees. Homogeneous second-phase precipitation. *Materials Science and Technology*, 1991.

[63] H. Wakeshima. Time lag in the self-nucleation. *The Journal of Chemical Physics*, 22(9):1614–1615, 1954.

[64] L. Xu, E. J. Bedrick, T. Hanson, and C. Restrepo. A comparison of statistical tools for identifying modality in body mass distributions. *Journal of Data Science*, 12(1):175–196, 2014.

[65] W. Yuan, A. Odjo, N. E. Sammons, J. Caballero, and M. R. Eden. Process structure optimization using a hybrid disjunctive-genetic programming approach. volume 27, pages 669–674. Elsevier, 2009.

[66] V. l. Zel'dovich, G. A. Sobyanina, and V. G. Pushin. Bimodal size distribution of Ti3Ni4 particles and martensitic transformations in slowly cooled nickel-rich TiNi alloys. *Scripta Materialia*, 37(1):79–84, Jul 1997.

[67] J. Zhang, W. Cai, X. Ren, K. Otsuka, and M. Asai. The nature of reversible change in Ms temperatures of Ti–Ni alloys with alternating aging. *Materials Transactions, JIM*, 40(12):1367–1375, 1999.

[68] N. Zhou, C. Shen, M.-X. Wagner, G. Eggeler, M. Mills, and Y. Wang. Effect of Ni 4 Ti 3 precipitation on martensitic transformation in Ti–Ni. *Acta Materialia*, 58(20):6685–6694, 2010.

APPENDIX A

EXAMPLE MATCALC SCRIPT

```
$*************************************************************************$
$*************************WORKSPACE*****************************************$
$*************************************************************************$

use-module core                         $ use the core module for all calculations
close-workspace f                       $ close any open workspaces in this instance
new-workspace                           $ open a fresh workspace in this instance

if (matcalc_version<5510004)            $ MatCalc version verification step
  send-dialog-string "MatCalc version must be 5.51.0004 or higher to run this script.
Stopping."
  stop_run_script                       $ stop script to avoid MatCalc crash
endif



$*************************************************************************$
$*********************DATABASE_AND_SYSTEM*********************************$
$*************************************************************************$

set-working-directory C:\Program Files (x86)\MatCalc $ specify location of MatCalc on
computer
open-thermodyn-database mc_sma_v1.000.tdb       $ select thermo database to read
select-elements Ni Ti                   $ select elements to consider during calculation
select-phases bcc_b2 Ti3Ni4             $ select phases to consider during calculation
read-thermodyn-database                 $ load thermodynamic data from database
read-mobility-database mc_ni2.004.ddb   $ load kinetic data from mobility database

set-reference-element Ti                $ set Titanium as the reference element
enter-composition xp Ni=52              specify nominal composition of Ni in system

set-temperature-celsius 23              $ set temperature for equilibrium calculation
set-automatic-startvalues               $ set standard values for equilibrium calc
calculate-equilibrium                   $ start equilibrium calculation
```

```
$*********************************************************************$
$**********************PRECIPITATION_SETUP**********************$
$*********************************************************************$

create-precipitation-domain austenite      $ set precipitation domain and name it austenite
set-precipitation-parameter austenite x bcc_b2        $ set precip domain phase
set-precipitation-parameter austenite t d e 1e11      $ set disl density to 1e11 [m/m3]
set-precipitation-parameter austenite t g 500e-6      $ set average grain diameter [m]

create-new-phase Ti3Ni4 p                  $ set a new precip. and name it Ti3Ni4
set-precipitation-parameter Ti3Ni4_p0 c 500           $ set max # distribution bins to 500
set-precipitation-parameter Ti3Ni4_p0 d austenite     $ set precips nucleation domain
set-precipitation-parameter Ti3Ni4_p0 n s f 3e29      $ set number of nucleation sites
set-precipitation-parameter Ti3Ni4_p0 t m y           $ set vol. misfit to automatic
set-precipitation-parameter Ti3Ni4_p0 n f y           $ consider volumetric misfit
set-precipitation-parameter Ti3Ni4_p0 z n             $ use specified interfacial energy
set-precipitation-parameter Ti3Ni4_p0 i n 0.0505      $ specify interfacial energy [j/m^2]
set-precipitation-parameter Ti3Ni4_p0 h y 0.24        $ set shape factor to 0.24
set-precipitation-parameter Ti3Ni4_p0 n g y $ account for GB energy during nucleation
set-precipitation-parameter Ti3Ni4_p0 n d 0.35e-9 $ set minimum nucleation radius [m]



$*********************************************************************$
$**********************HEAT_TREATMENT_SETUP*******************$
$*********************************************************************$

create_heat_treatment HT1                  $  new heat treatment
append_ht_segment HT1                      $ create a heat treatment segment
edit-ht-segment HT1 . d n austenite        $ define austenite as precip domain
edit_ht_segment HT1 . s 23                 $ set start temperature [C]
edit_ht_segment HT1 . 3 550 300            $ set 1st stage temp and time to reach it [C] [s]
edit-ht-segment HT1 . R +set-precipitation-parameter Ti3Ni4_p0 n s n $ nuc. off
edit-ht-segment HT1 . O +set-precipitation-parameter Ti3Ni4_p0 n s f 3e29 $ nuc. on

append-ht-segment HT1                      $ create next heat treatment (1st stage)
edit-ht-segment HT1 . 3 550 3600           $ hold at 1st aging temperature for 2 hours

append-ht-segment HT1                      $ create next heat treatment stage (ramp down)
edit-ht-segment HT1 . 3 250 5              $ set 2nd stage temp and time to reach it
edit-ht-segment HT1 . R +set-precipitation-parameter Ti3Ni4_p0 n s n $ nuc. off
edit-ht-segment HT1 . O +set-precipitation-parameter Ti3Ni4_p0 n s f 3e29 $ nuc. on
```

```
append-ht-segment HT1                  $ create next heat treatment (2nd stage)
edit-ht-segment HT1 . 3 250 18000      $ hold at 2nd aging temperature for 5 hours



$*********************************************************************$
$************************CREATE_PLOTS*****************************$
$*********************************************************************$
This section does not effect the model progression. It is purely for creating GUI
windows

new-gui-window p1
set-variable-value plot_frame active_frame_ID
set-gui-window-property . x stepvalue
set-gui-window-property . s u y
set-gui-window-property . s t time [s]
set-gui-window-property . n 2

set-plot-option . s n b t$c
set-plot-option . a y 1 t Temperature [C]

create-new-plot x .
set-plot-option . s n b f_prec$*
set-plot-option . a y 1 t phase fraction
set-plot-option . a y 1 s 1e-4..1
set-plot-option . l a y
set-plot-option . a y 1 y log

create-new-plot x .
set-plot-option . s n b d_vmean$*
set-plot-option . a y 1 t Mean Dia [microns]
set-plot-option . a y 1 f 1e6
set-plot-option . l a y
set-plot-option . a y 1 y log

create-new-plot x .
set-plot-option . s n b num_prec$*
set-plot-option . a y 1 t number density [m<sup>-3</sup>]
set-plot-option . a y 1 s 1e9
set-plot-option . l a y
set-plot-option . a y 1 y log

move-gui-window . 50 50 640 850
```

```
update-gui-window .

new-gui-window p5
set-plot-option . s n p Ti3Ni4_p0
set-plot-option . a x 1 f 1e6
set-plot-option . a x 1 t Dia [microns]
set-plot-option . a x 1 y log
set-plot-option . h t n
set-plot-option . a x 1 s auto
set-plot-option . a y 1 s auto
set-plot-option . a y 1 y log
set-plot-option . a y 1 t number density  [m<sup>-3</sup>]

move-gui-window . 200 200 640 850
update-gui-window .



$**********************************************************************$
$************************START_SIMULATION**************************$
$**********************************************************************$

set-simulation-parameter e 1e24          $ set maximum allowable calculation time [s]
set-simulation-parameter i a 1e-4 1e+2   $ set minimum and maximum time step [s]
set-simulation-parameter t h HT1 10      $ specify heat treatment from above to analyze
set-simulation-parameter s r             $ ignore previously calculated precipitates
start-precipitate-simulation             $ start the simulation



$**********************************************************************$
$************************EXPORT_VARIABLES**************************$
$**********************************************************************$
This section formats and exports sets of single value metrics to a text file for further
analysis.

export-open-file
/home/lukejohnson/Desktop/Dropbox/Lab/Research/NiTi/NOMAD/output_file.txt
export-file-variable "  StepValue      t$c          f_prec$Ti3Ni4_p0
d_vmean$Ti3Ni4_p0      num_prec$Ti3Ni4_p0
export-file-buffer "  %.3e      %.2f       %.3e            %.3e            %.3e" StepValue t$c
f_prec$Ti3Ni4_p0 d_vmean$Ti3Ni4_p0 num_prec$Ti3Ni4_p0
export-close-file
```

```
$**********************************************************************$
$**********************EXPORT_DISTRIBUTION**********************$
$**********************************************************************$
This section exports the precipitate size distribution of the heat treatment simulation.

export-precipitate-dist Ti3Ni4_p0
/home/lukejohnson/Desktop/Dropbox/Lab/Research/NiTi/NOMAD/output_dist.txt
```